Development and experimental validation of a humanoid pedestrian model that captures stepping behavior and body rotation

Xiaoyun Shang[1], Rui Jiang[1,*], S.C.Wong[2,*], Ziyou Gao[1] and Wenguo Weng[3]

[1]*School of Systems Science, Beijing Jiaotong University, Beijing 100044, PR China*

[2]*Department of Civil Engineering, The University of Hong Kong, Pokfulam Road, Hong Kong, PR China*

[3]*School of Safety Science, Tsinghua University, Beijing ,100084, P.R. China*

Abstract:

This paper presents a novel humanoid pedestrian model (HPM) incorporating stepping behavior and body rotation. The HPM is composed of two main components: (a) body modeling and (b) gait planning. A pedestrian is represented as a three-dimensional skeleton with 11 degrees of freedom in the body modeling component, which provides a universal approach for explaining the mathematical correlations between joint rotation angles and critical gait parameters such as step length, step width, and projected shoulder width. A framework for designing gaits that accounts for step-synchronization behavior and the effect of body rotation on stepping behavior is offered by the gait planning process. To validate the model, two types of experiments were conducted: nine sets of single-file experiments and 10 sets of bidirectional flow experiments, in which pedestrians walked in a 0.5-m-wide circular corridor and rotated their bodies to avoid collisions. It was suggested by the fundamental diagrams that body rotation reduces the walking speed of a pedestrian and consequently affects the overall flow rate. Furthermore, it was found that pedestrians were more resistant to moving forward in narrow bidirectional flow environments and tend to wait for a larger gap in front to take a longer or faster step.

* Corresponding authors.
E-mail addresses: jiangrui@bjtu.edu.cn (R. Jiang), hhecwsc@hku.hk (S.C. Wong).

This behavior led to the formation of stop-and-go waves in the narrow-corridor scenario. The simulation results were consistent with the experimental findings in terms of flow-density relationships and the reproduction of stop-and-go waves. Additionally, synchronized steps were detected in the simulation and quantitatively compared with a publicly available dataset. The HPM offers a new perspective on modeling pedestrian dynamics and emphasizes the necessity of accounting for micro-characteristics at the step level in pedestrian models.

Keywords: humanoid pedestrian model, stepping behavior, body rotation, step synchronization, stop-and-go waves

1. Introduction

Pedestrian flow exhibits many interesting phenomena, such as lane formation (Bacik et al., 2023; Dietrich and Köster, 2014; Helbing and Molnár, 1995; Murakami et al., 2021), turbulence (Helbing et al., 2007; Johansson et al., 2012), and the "fast-is-slow" effect (Helbing et al., 2000). Moreover, crowding pedestrians is dangerous, as it may lead to serious trampling accidents (Alaska et al., 2017; Burkle and Hsu, 2011). For example, on October 29, 2022, a pedestrian stampede occurred during a Halloween gathering in Itaewon, Korea, resulting in the tragic loss of at least 159 lives and leaving 196 others injured (https://en.wikipedia.org/wiki/Seoul_Halloween_crowd_crush). Extensive efforts have been made over the past few decades to understand pedestrian flow dynamics and thereby determine how to prevent such tragedies, and researchers have focused on determining the behavior of pedestrians from physical and biological perspectives (Guo et al., 2016; Haghani and Sarvi, 2018; Helbing et al., 2000; Helbing et al., 2005; Hoogendoorn and Daamen, 2005; Moussaïd et al., 2011; Murakami et al., 2021; Nicolas et al., 2017; Nikolić et al., 2019).

Many models have been devised to reproduce the observed phenomena of pedestrian flow. Typical

models are continuum models (Liang et al., 2021; Wageningen-Kessels et al., 2018), cellular automata (CA) models (Blue and Adler, 2001; Kirchner and Schadschneider, 2002), and social force models (SFM) (Helbing et al., 2000; Helbing and Molnár, 1995), which have been widely studied and used in practice. CA models and the SFM are particle-based models (Huang et al., 2018), wherein a pedestrian is considered to be an indivisible whole, jumping or sliding smoothly from cell to cell. However, in recent years, researchers have realized the inaccuracy of particle-based models and have instead focused on examining the micro-characteristics of human walking. In particular, stepping and body rotation behavior have been widely investigated, as described below.

Stepping behavior: The stepping behavior of pedestrians has been examined using single-file experiments (Fang et al., 2012; Jelić et al., 2012b; Ma et al., 2018, 2021; Wang et al., 2018; Zeng et al., 2018), and some crucial characteristics of stepping behavior, such as step length, step width, and step duration, have been investigated. This has revealed vital relationships, such as those between step length and headway, step frequency (the reciprocal of step duration) and headway, and step length and velocity. Moreover, step-synchronization has been studied (Jelić et al., 2012b; Ma et al., 2018, 2021; Wang et al., 2018). Step-synchronization occurs under specific circumstances and involves pedestrians adjusting their step phase to match that of their leaders, which results in more efficient use of space than step non-synchronization. Experiments indicate that step-synchronization is most likely to be triggered when the flow rate of pedestrians reaches a maximum value (Ma et al., 2021).

Stepping behavior has also been incorporated into many models, some of which consider step length or step duration but model a pedestrian as an indivisible whole. Chraibi et al. (2010) devised a generalized centrifugal-force model in which the SFM controls elliptical pedestrians and move smoothly. The major-axis of an ellipse represents step length, while the minor-axis represents lateral

sway. Seitz et al. (2015), Seitz and Köster (2012), and von Sivers and Köster (2015) developed the optimal step model (OSM), in which a pedestrian seeks the next step on a disc with a radius equal to the maximum step length. The step duration and the maximum step length are set based on free-walking experiments. However, although the OSM model allows pedestrians to adapt their step length, the step duration is fixed, which is inconsistent with actual stepping behavior. Fang et al. (2012) and Zeng et al. (2018) have introduced randomicity into a step frequency and headway formula. However, the randomicity incorporated into their models may cause unrealistic phenomena, such as sudden stops and extreme congestion.

The above-mentioned models do not consider which foot a pedestrian is stepping forward with, so these models are unable to reproduce step-synchronization. The biped model devised by Huang et al. (2018) characterizes a pedestrian as two vectors that represent the pedestrian's feet. However, although step-synchronization is captured qualitatively in this model, the quantitative comparability of its results with experimental results needs to be improved.

Body rotation: Body rotation is essential for collision avoidance in narrow corridors and high-density situations (Jin et al., 2017; Nakatsuka et al., 2019; Song et al., 2019; Yamamoto et al., 2019). Su et al. (2019) extended the SFM by adjusting the radii of circular pedestrians in narrow-corridor scenarios. Several studies have modeled pedestrians as various asymmetric shapes. For example, Jin et al. (2017) and Miyagawa and Ichinose (2020) have developed the CA model, in which one pedestrian occupies two cells. As a result, there are two rotation angles—0° and 90°—so the deadlock of the counterflow is mitigated. Furthermore, researchers have utilized various geometric shapes such as ellipses (Farina et al., 2017; Xu et al., 2019), spheropolygons (Alonso-Marroquín et al., 2014), and multi-circles (Langston et al., 2006) to represent pedestrians. A torque model with spherocylinders

(Hidalgo et al., 2017) and three-circle pedestrians (Song et al., 2019) has also been developed based on the SFM. This model effectively simulates the rotation behavior of pedestrians passing through a narrow exit. Best et al. (2016) and Narang et al. (2017) developed a model that uses velocity obstacles, including collision avoidance and multiple elliptical pedestrians. Yamamoto et al. (2019) devised a rule-based model to describe body rotation in a narrow corridor and identified the impact of rotation angle on the velocity of a pedestrian.

Research gap: In the above-mentioned studies, stepping and body rotation behavior have been studied separately. However, these two behaviors are closely correlated, as body rotation intrinsically determines stepping behavior[1]. For example, it is evident that when the body rotates clockwise, stepping forward with the right foot is more challenging than doing so with the left foot.

Motivated by this research gap, a humanoid pedestrian model (HPM) that simulates the human walking process was first developed using three-dimensional (3D) skeletal pedestrians. In the HPM, pedestrians can avoid conflict through body rotation, and its impact on stepping behavior naturally occurs through the 3-D skeleton. Moreover, stepping behavior, including step length, step width, and step duration, is thoroughly examined.

To validate the developed model, single-file and bidirectional-flow experiments in a narrow circular corridor were conducted. The step-synchronization is quantitatively compared with that reported by Ma et al. (2021) to validate the model further.

The rest of the paper is organized as follows. Section 2 presents the HPM. Section 3 offers the experimental setup and the results. Section 4 gives the simulation results, and Section 5 concludes the

[1] To provide clarification, when "stepping while rotating" occurs, changes in the walking state and step width may take place, potentially having a significant impact on the maximum step length and step duration. Moreover, step synchronization always exists, regardless of whether body rotation is present or not.

paper.

2. HPM

This section introduces the HPM, which represents a pedestrian as a multi-link system with a three-dimensional (3D) skeleton and 11 degrees of freedom (DoFs). The state of a pedestrian $ped \in \mathbb{P}$ is generally defined as follows:

$$ped = \langle P, X, \Delta, S \in \{N, D, E\} \rangle \tag{1}$$

where $P \in \mathbb{R}^{3\times|J|}$; $|J|$ is the number of joints, with each joint position described by a 3D vector; $P^j(t)$ is the position of the jth joint at time t; and $X = [l, w, s, \gamma, \omega]^T$ is a set of five vital gait parameters, which are briefly defined in Table 1 and described in Section 2.1.1. Δ is the step duration, and S is an indicator of the body rotation difficulty, where N, D, and E represent "normal," "difficult," and "easy" walk, respectively.

Table 1 Definitions of gait parameters for pedestrian i (ped_i).

Gait parameter	Definition
$\boldsymbol{T_i^n}$	Start (stand) moment of the nth step
$\boldsymbol{\Delta_i^n}$	Duration of the nth step
$\boldsymbol{P_i(t)}$	Set of all joint positions at time t
$\boldsymbol{C_i(t)}$	Position of the center of mass at time t
$\boldsymbol{l_i(t)}$; $\boldsymbol{l_i^n}$	Step length at time t; step length of the nth step
$\boldsymbol{w_i(t)}$; $\boldsymbol{w_i^n}$	Step width at time t; step width of the nth step
$\boldsymbol{s_i(t)}$; $\boldsymbol{s_i^n}$	Projected shoulder width at time t; projected shoulder width of the nth step
$\boldsymbol{\omega_i}$	Sway angle
$\boldsymbol{\gamma_i^n}$	Orientation of the nth step
$\boldsymbol{F_i^{st}}$; $\boldsymbol{F_i^{sw}}$	Support foot; swing foot
$\boldsymbol{S_i^n}$	Walking state of the nth step

First, a step consists of a single support phase followed by a double support phase. During the single support phase, one foot (i.e., the swing foot, F^{sw}) swings forward while the other (i.e., the support

foot, F^{st}) remains fixed on the ground. During the double support phase, both feet are in contact with the ground, and the center of mass shifts from the support foot to the swing foot.

In the HPM, the double support phase is simplified as a standing moment, which signifies the moment at which one foot leaves the ground as the other foot contacts the ground. Thus, the step duration Δ is equivalent to the duration of the single support phase. The temporal structure of the HPM is depicted in Fig. 1, and the temporal parameters are defined in Table 1.

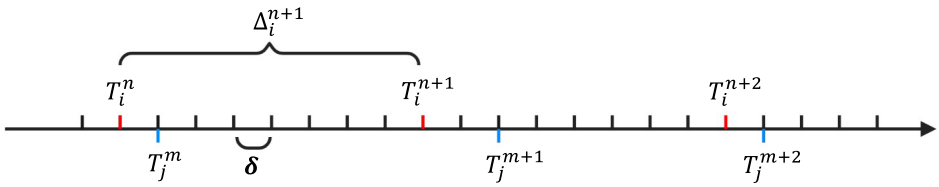

Fig. 1. Temporal structure of the HPM, where i and j represent two pedestrians, and δ is the time step.

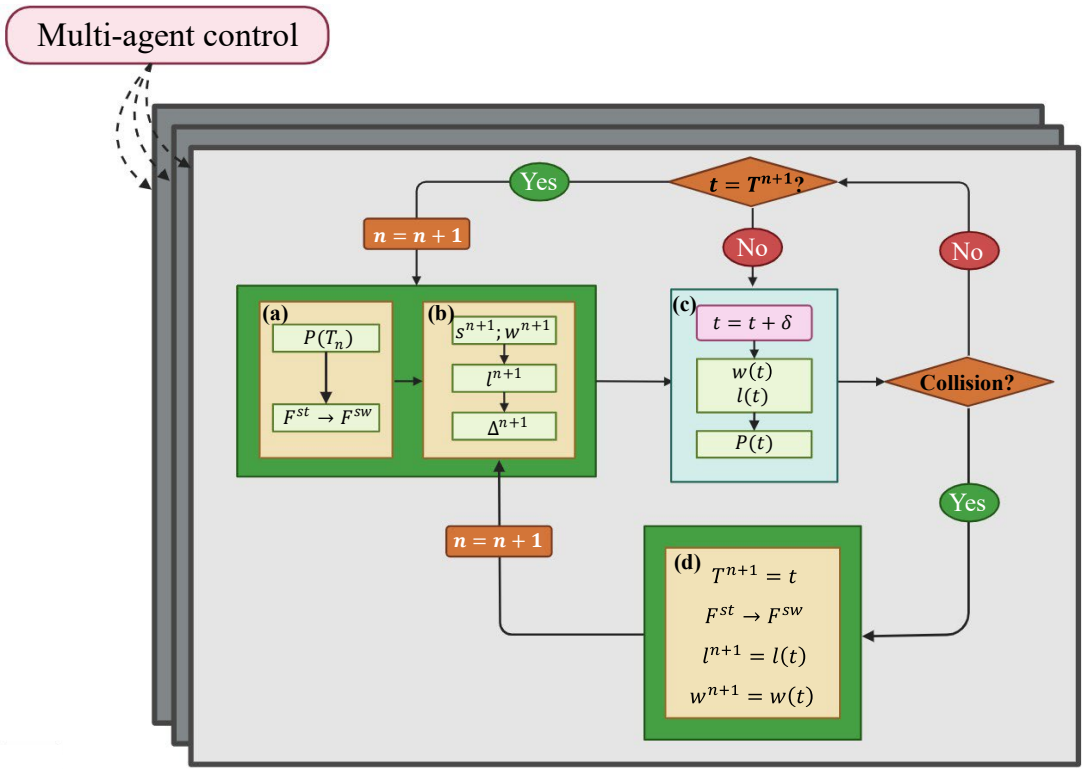

Fig. 2. Overview of the HPM framework. The double support phase is indicated by the green boxes, while the single support phase is indicated by the cyan box

Figure 2 illustrates the HPM framework, in which the time intervals are defined as $t = t + \delta$, where δ is the time step. When a pedestrian completes the nth step, the body joint positions $P(T_n)$ are

calculated, and the support foot is switched (Fig. 2(a) and Section 2.1). The certain gait parameters of the $n+1$th step, X^{n+1}, are then planned sequentially (Fig. 2(b), Section 2.2 and Section 4.1). During the single support phase, the swing foot moves forward according to the predetermined rules (Fig. 2(c) and Section 2.3.1), and the body joint positions are calculated at each time step (Fig. 2(c) and Section 2.1). In addition, a collision avoidance mechanism is designed (Fig. 2(d) and Section 2.3.2).

Considering the initial phase of the HPM, this study focuses on one-dimensional (1D) walking behavior, i.e., the behavior of pedestrians walking along a predetermined route. Modeling of the two-dimensional (2D) walking behavior, i.e., the determination of both the walking speed and direction, will be addressed in future work.

2.1. Body modeling

In the HPM, a pedestrian is represented not as a particle but a 3D skeleton composed of several rigid links connected by revolute joints, see Fig. 3(a). This multi-link system has 11 DoFs, including one DoF at the waist, six DoFs at the pelvis, and four DoFs at the ankles (Fig. 3(c)). For simplicity, the movement of the knees and arms is not modeled, as this movement does not significantly impact the gait of a pedestrian, which is primarily determined by the placement of the feet at the standing moment.

In the HPM, the lower and upper body joint positions under the absolute coordinate system (ACS) are calculated separately. This process involves the following steps (Steps 1–3 in Fig. 3(c)). During walking, the support foot remains fixed on the ground in a constant position. To begin, the absolute coordinate of the support foot, P^0, is determined. Next, utilizing the Denavit-Hartenberg (DH) convention (Denavit and Hartenberg, 1955), the joint position of the lower body is calculated from P^1 to P^5, based on P^0. Finally, by performing coordinate translation, the joint coordinates of the upper body (P^7–P^{10}) are computed relative to the center point of the pelvis, P^6 (indicated by the green point

in Fig. 3(c)). The notation $P_i^6(t)$ refers to $C_i(t)$.

The length of the links in Fig. 3, which represent human body parameters, are provided in Table 2, which are sourced from Faraji and Ijspeert (2017)[2]. The shoulder width data is acquired from Song et al. (2019)[3]. H is human height.

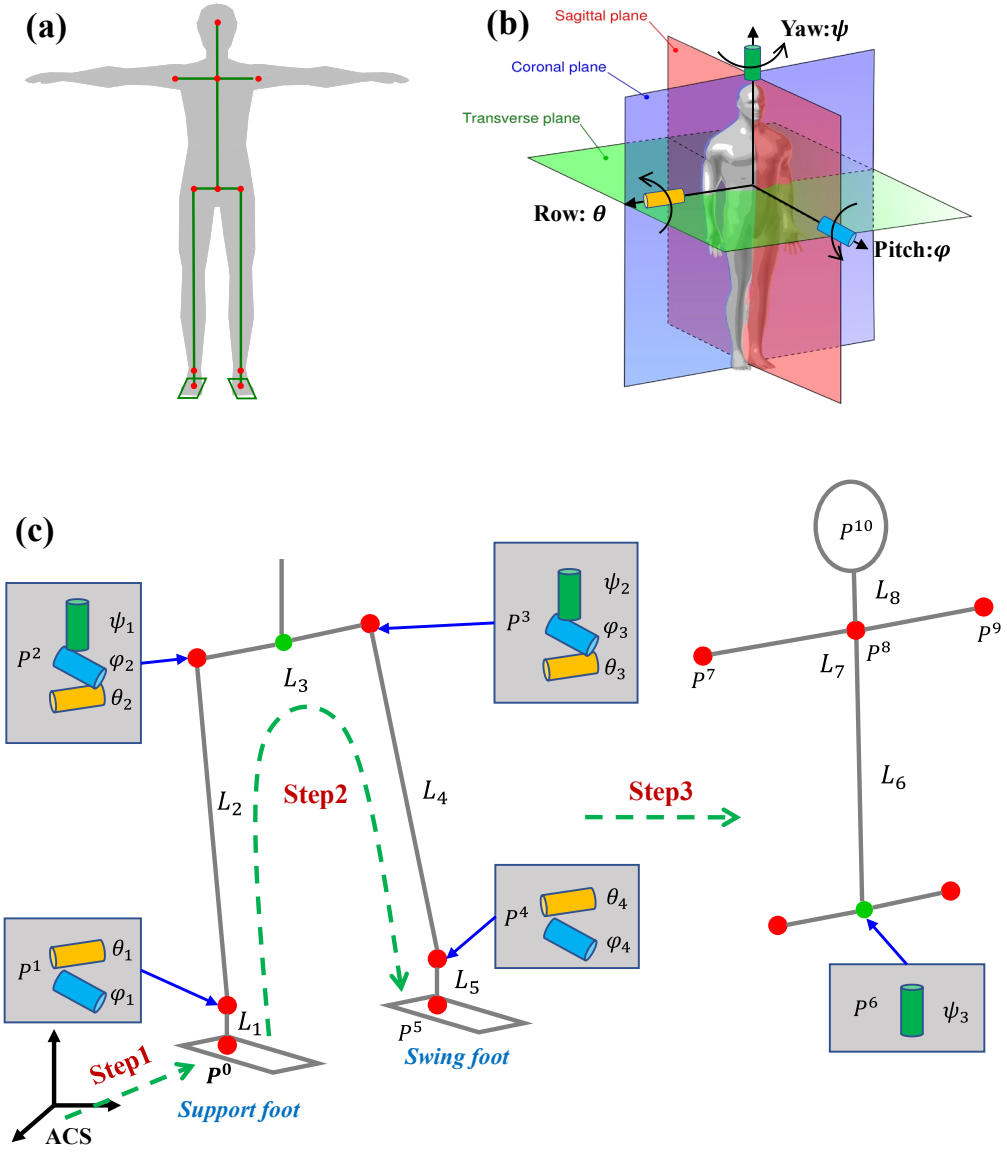

Fig. 3. (a) This figure provides an overview of the 3D skeleton. (b) The three Euler angles $\psi, \theta,$ and φ and their respective positive directions are defined. (c) The joints are numbered, the degrees of freedom are distributed, and the calculation order is determined. These definitions in (b) are taken from https://commons.wikimedia.org/w/index.php?title=File:Human_anatomy_planes.svg&oldid=448399308 (last visited April 4, 2023).

[2] These values are available in their open-source code.
[3] In their paper, the authors set the shoulder width to 0.45 m. It is assumed that the shoulder width is proportional to human height, which is taken as 1.7 m in this context. Therefore, for a person with a height of H, their shoulder width can be calculated as$(0.45 \,/\, 1.7) \times H$.

Table 2 Adult human body parameters.

Body part	Parameter	Value
Left, right ankle	$L_1; L_5$	$0.0451H$
Left, right leg	$L_2; L_4$	$0.4791H$
Pelvis	L_3	$0.1176H$
Trunk	L_6	$0.3495H$
Shoulder	L_7	$0.2647H$
Neck	L_8	$0.1396H$

2.1.1. Definitions of gait parameters

Some parameters used in this section are provided and explained in Table 3.

Table 3 Some parameters in Section 2.1.1 and its definition

Parameter	Definition
$\boldsymbol{\theta_{1\sim4}}$	The set $\{\theta_1, \theta_2, \theta_3, \theta_4\}$, whose definitions is in Fig.3(c)
$\boldsymbol{\psi_{1\sim3}}$	The set $\{\psi_1, \psi_2, \psi_3\}$, whose definitions is in Fig.3(c)
$\boldsymbol{\varphi_{1\sim4}}$	The set $\{\varphi_1, \varphi_2, \varphi_3, \varphi_4\}$, whose definitions is in Fig.3(c)
$\boldsymbol{l^{max}}$	Maximum step length
$\boldsymbol{l^F}$	Free-walking step length
$\boldsymbol{\theta_w^{max}}$	Maximum stepping angle
$\boldsymbol{L^p}$	Pelvis length
$\boldsymbol{L^l}$	Leg length
$\boldsymbol{\psi_p}$	Pelvis rotation angle
$\boldsymbol{\psi_s}$	Shoulder rotation angle

As depicted in Fig. 3(c), the human gait can be described with a set of links and three orthogonal rotation angles, i.e., Euler angles. The link lengths are fixed, and a specific set of rotation angles corresponds to a particular gait. Additionally, the gait of a pedestrian can be described using five gait parameters X: step length (l), projected shoulder width (s), step width (w), lateral sway angle (ω) (Kuo, 1999), and orientation (γ). The definitions of l, w, s, ω, and γ are illustrated in Fig. 4. There exists an equivalent mapping from the three rotation angles to five physical variables, defined as $\{l, w, s, \gamma, \omega\} \overset{\mathcal{B}}{\rightarrow} \{\theta_{1\sim4}, \psi_{1\sim3}, \varphi_{1\sim4}\}$. A gait that corresponds to these five variables is denoted by $\mathcal{B}(X)$.

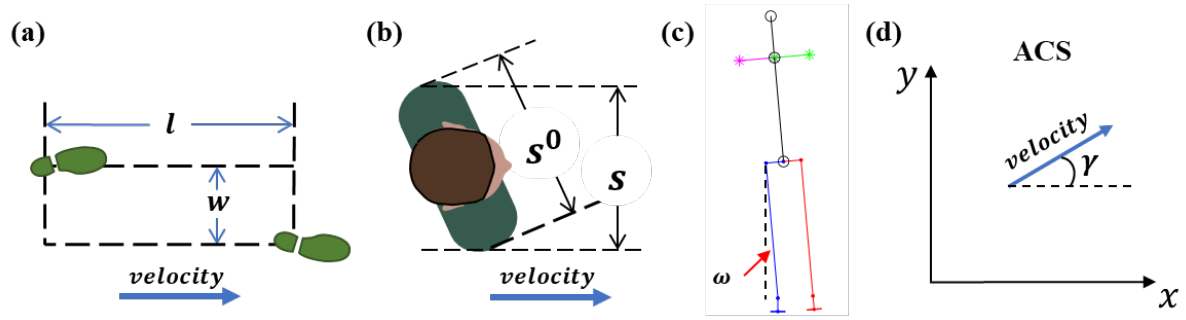

Fig. 4. (a) Definitions of l and w. (b) Definition of s, where s^0 is the shoulder width. (c) Definition of ω. (d) Definition of γ; x- and y- axes belong to the ACS. (a) and (b) are superior views, and (c) is an anterior view.

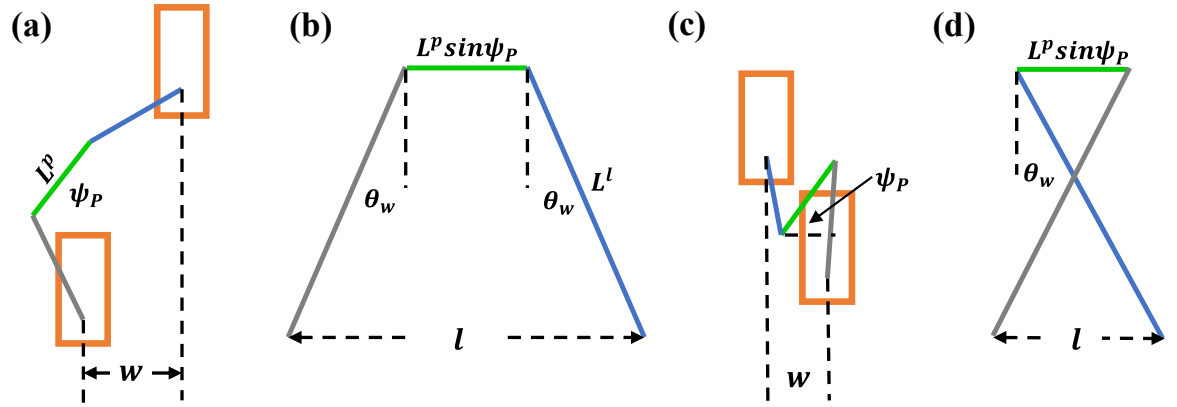

Fig. 5. Two walking states: (a), (b) E-walk state; (c), (d) D-walk state. (a), (c) Superior view; (b), (d) lateral view, in which the pedestrian moves to the right. In all subfigures, the gray and blue lines represent the support leg and swing leg, respectively.

Three types of walking states, $S \in \{N, D, E\}$, are defined below. The walking state can be classified as "Normal-walk" (N) when a pedestrian walks without body rotation. However, when a pedestrian walks and rotates the body in a counterclockwise (clockwise) direction, it is more convenient for them to step forward with the right (left) foot. This is demonstrated in Figures 5(a) and (b). According to the projection of the pelvis in the velocity direction, the maximum step length l^{max} in this situation may be larger than the maximum step length without rotation, and it is denoted by the free-walking step length l^F. This walking state corresponds to state E. Similarly, when a pedestrian walks in a counterclockwise (clockwise) direction, it is more challenging for the pedestrian to step forward with the left (right) foot, as shown in Figs. 5(c) and (d). In this situation, l^{max} may be shorter than l^F. This walking state corresponds to state D. If a pedestrian does not change direction, the walking state S alternates between E and D. The step length is related to the step width during rotation. To quantify states E and D, the maximum stepping angle θ_w^{max} is assumed to be a constant.

Table 4 lists the values of θ_w in the three walking states. Table 5 lists the joint rotation angle values, where L (R) indicates the left (right) foot support scenario. l_i^F and $\theta_{i,w}^{max}$ represent the l^F and θ_w^{max} values of ped_i, respectively. $L^{p'} = L^p\, sin\psi_p$ denotes the projection of the pelvis in the velocity direction. The pelvis and shoulder rotation angles are $\psi_p = \arccos(w/L^p)$ and $\psi_s = \arccos(s/s^0)$, respectively. L^p is the pelvis width, and L^l is the leg length (Fig. 5). L^p, L^l, and s^0 are equivalent to L_3, L_2 (L_4), and L_7 in Fig. 3(c) and Table 2, respectively.

The turning behavior can be described by the variation in the orientation $\Delta\gamma$. The orientation of the $n+1$th step is $\gamma^{n+1} = \gamma^n + \Delta\gamma$.$\Delta\gamma$ is determined by the curvature radius and center of the turn, where R_w is the radius of the curve in which the swing foot is located:

$$\Delta\gamma = \frac{l}{R_w} \tag{2}$$

Table 4 Values of θ_w for pedestrian i in the three walking states.

Parameter	Value		
	N	E	D
l^{max}	l_i^F	$l_i^F + L_i^{p'}$	$l_i^F - L_i^{p'}$
θ_w^{max}	$\theta_{i,w}^{max}$	$\theta_{i,w}^{max}$	$\theta_{i,w}^{max}$
θ_w	$\arcsin\left(\frac{l}{2L^l}\right)$	$\arcsin\left(\frac{l-L^{p'}}{2L^l}\right)$	$\arcsin\left(\frac{l+L^{p'}}{2L^l}\right)$

Table 5 Joint rotation angles.

θ	Value	φ	Value (L)	Value (R)	ψ	Value
θ_1	θ_w	φ_1	$-\omega$	ω	ψ_1	$\psi_R + \Delta\gamma$
θ_2	$-\theta_w$	φ_2	0	0	ψ_2	$-\psi_R$
θ_3	$-\theta_w$	φ_3	$\pi/2$	$-\pi/2$	ψ_3	$\psi_S - \psi_p$
θ_4	θ_w	φ_4	ω	$-\omega$	---	---

2.2. Double support phase

As mentioned, the gait of a pedestrian in the next step is planned during the double support phase. This section discusses the determination of the gait parameters, i.e., the projected shoulder width, step width, step length, and step duration.

2.2.1. Step width

As mentioned in Section 2.1.1, the step length is related to the step width during rotation. Thus, the step width must be calculated before the step length. Body rotation is a shoulder-dominated movement. It is assumed that the shoulder rotation angle determines the pelvis rotation angle, i.e., the step width is obtained from the projected shoulder width. Based on this assumption, a pedestrian is modeled as a line of length $2a$.

A simple scenario is considered. Pedestrian ped_i, who completes the nth step at time t ($t = T_i^n$), is walking in the direction opposite to that of other pedestrians and may collide with some of them within a few seconds. The pedestrians maintain their walking directions and can avoid conflict only by rotating their bodies.

First, when the distance between the pedestrians is sufficiently small ($0 < \left[\vec{d}_{ij}\right]_{\vec{v}_i} \leq \xi_1$), ped_i must rotate their body to avoid a collision with a front pedestrian ped_j. Here, $\left[\vec{d}_{ij}\right]_{\vec{v}_i} = \vec{d}_{ij} \cdot \vec{v}_i / \|\vec{v}_i\|$ is the value of $\vec{V}_1$ projected onto the direction of $\vec{V}_2$. $\vec{d}_{ij} = \vec{C}_j(t) - \vec{C}_i(t)$. $\xi_1 = \max\left(d_{th}, k\, l_i^n, k\, l_j^m\right)$ is a distance determined by the step lengths of ped_i and ped_j, which indicates that they will collide in k steps if their step lengths do not change. l_j^m is the previous step length of ped_j ($t \in \left(\mathrm{T}_j^m, T_j^{m+1}\right)$), and d_{th} is a threshold distance.

Additionally, if ped_j is behind ped_i after passing but the distance between them is small ($0 \leq -\left[\vec{d}_{ij}\right]_{\vec{v}_i} \leq \xi_2$), the gait of ped_i cannot be immediately restored. Thus, rotation must be performed in this situation as well. Here, ξ_2 is set as the body depth $2b$ (Yamamoto et al., 2019).

The shoulder rotation angle for ped_i must be sufficiently large to avoid all potential collisions. Therefore, the minimum passing gap d_i is determined. If the body rotation is simplified as a fixed-axis rotation around the center of mass, then d_i is half the projected shoulder width s_i^{n+1}:

$$d_i = \frac{1}{2}s_i^{n+1} = \max\left(0, \min_{ped_j \in \mathbb{P}, j \neq i}\left\{\mathcal{D}\middle| -\xi_2 \leq \left[\vec{d}_{ij}\right]_{\vec{v}_i} \leq \xi_1\right\}\right) \tag{3}$$

In the model, d_i is assumed to be determined by the general function $\mathcal{D}(\cdot)$ (analogous to the general function of the flow rate versus density in the fundamental diagram of traffic flow), which must be specified in the simulation. The psychological tendency of ped_i to avoid physical contact with others should also be considered in $\mathcal{D}(\cdot)$. One specific form of $\mathcal{D}(\cdot)$ is presented in Section 4.1.

A shoulder can be rotated up to an angle of 90° ($s = 0$). However, it is impossible for the pelvis to be rotated at such a large angle while walking. Therefore, the maximum pelvis rotation angle ψ_p^{max} is limited. Overall, the width of the $n+1$th step (w_i^{n+1}) can be calculated as follows:

$$w_i^{n+1} = \max\left(L_i^p \frac{s_i^{n+1}}{s_i^0}, L_i^p \cos\psi_p^{max}\right) \tag{4}$$

2.2.2. Step length

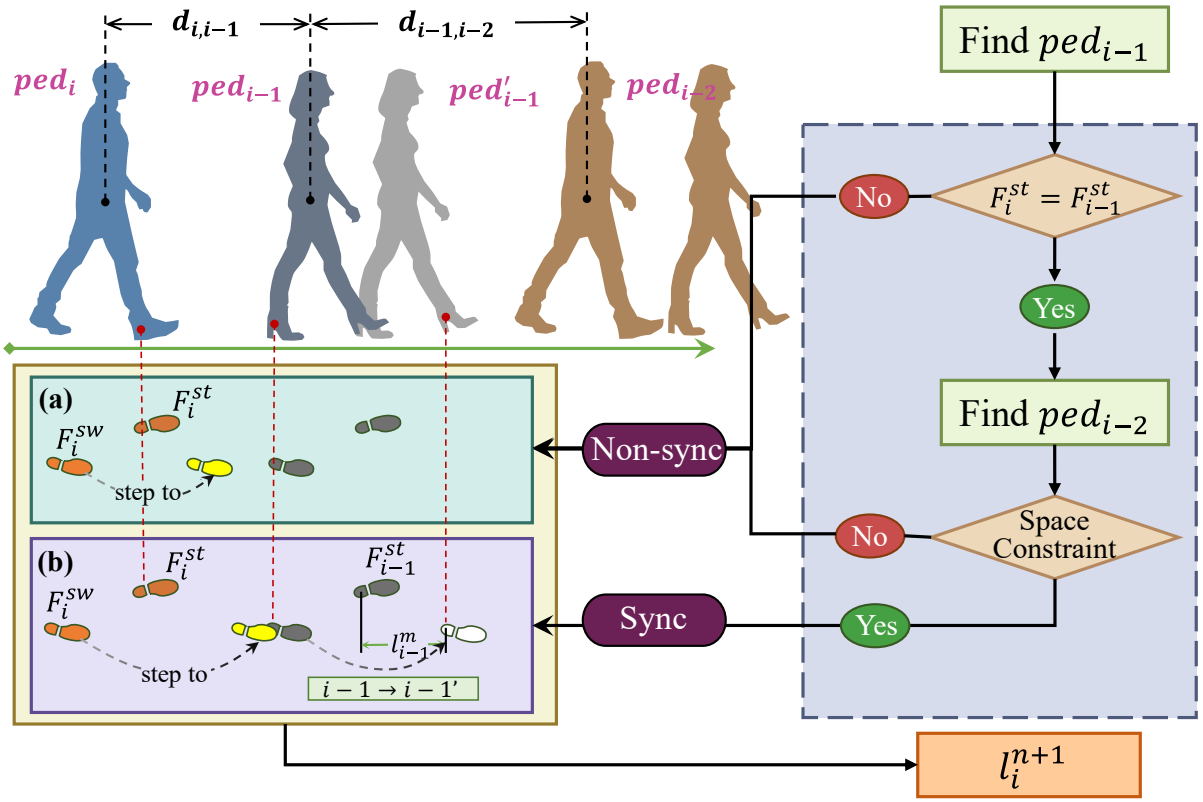

Fig. 6. Framework for calculating the step length for situations involving (a) non-step-synchronization and (b) step-synchronization.

Intuitively, the length of the next step of a pedestrian is primarily influenced by any obstacles

in the walking direction. Generally, the relative position of two successive pedestrians directly influences the step length of the following pedestrian.

Previous studies have demonstrated the existence of step-synchronization in single-file experiments (Jelić et al., 2012b; Ma et al., 2021; Wang et al., 2018). Step-synchronization is a unique self-organization phenomenon in which, under certain conditions, pedestrians actively adjust their step phase to match that of their leaders, i.e., they allow their swing leg to fill the gap left by the swing leg of their leaders. This organization results in more efficient use of space than non-step-synchronization. Step-synchronization requires followers to anticipate the movement of their leaders. As demonstrated in Fig. 6, ped_i must take a small step to avoid colliding with the leader ped_{i-1} when the distance between them is small (Fig. 6(a)). However, if ped_i can infer that the leader will continue moving forward based on the environment, ped_i can take a larger step without the risk of a collision (Fig. 6(b)).

Notably, the existing step-synchronization experiments have been limited to single-file scenarios. Thus, it is currently unknown whether step-synchronization exists in higher-dimensional scenarios, and, if it does, the manner in which steps are synchronized in these scenarios. Due to these limitations, the devised method for calculating the step length is applicable only to the scenarios, in which all pedestrians are in a line and their left (right) feet are aligned. For example, ped_i in Fig. 6 illustrates step-synchronization-inducing conditions and the method for calculating l_i^{n+1} when these conditions are met (Fig. 6(b)).

The first condition for two successive pedestrians to synchronize is that their swing foot must be the same at time t. Otherwise, the swing foot of ped_i (F_i^{sw}) may collide with the support foot of ped_{i-1} (F_{i-1}^{st}), as the support foot is fixed on the ground, while the swing foot is moving forward.

The second condition (space constraint) is that sufficient space is available for a leader to move

forward during the next step. This condition is specified as $d_{i-1,i-2} \geq \max(d_{safe}, l_{i-1}^m)$, where ped_{i-2} is the leader of ped_{i-1}, $d_{i-1,i-2}$ is the distance between ped_{i-1} and ped_{i-2}, and d_{safe} indicates the minimum safe distance required for ped_{i-1} to move forward, and l_{i-1}^m is the previous step length of ped_{i-1}. Then, l_i^{n+1} can be defined as:

$$\mathcal{F}' = \mathcal{F} + \mathbb{I}\left[F_i^{st} = F_{i-1}^{st}, d_{i-1,i-2} \geq \max(d_{safe}, l_{i-1}^m)\right] l_{i-1}^m \tag{5a}$$

$$l_i^{n+1} = \begin{cases} 0, & \mathcal{F}' < l_i^{min} \\ \min(l_i^{max}, \mathcal{F}'), & \mathcal{F}' \geq l_i^{min} \end{cases} \tag{5b}$$

where $\mathbb{I}[A]$ is an indicator function that equals 1 when A occurs and 0 when A does not occur. The value of l^{max}, which is influenced by the step width and the walking state, is provided in Table 4. The term l^{min} reflects pedestrians' preference for a longer, or a more comfortable step rather than immediately opting for a minimal step. $\mathcal{F}(\cdot)$ is a general function that determines the effective foot distance between two successive pedestrians. The specific forms of $\mathcal{F}(\cdot)$ and l^{min} will be presented in Section 4.1.

The necessity of setting step-synchronization should be emphasized. As demonstrated in Appendix A, a significant decrease in maximum flow rate can be observed if pedestrians do not synchronize their steps with their leaders.

2.2.3. Step duration

According to the results of single-file experiments, the step duration tends to increase as the headway (Fang et al., 2012; Zeng et al., 2018) or velocity (Wang et al., 2018) decreases. However, a high degree of variability in the step duration has also been observed (Fig. B1). Therefore, the step duration cannot be accurately defined using a specific equation and must be calculated by incorporating an element of randomness.

Intuitively, pedestrians tend to maintain a stable velocity in open spaces, with negligible fluctuations in step duration and length. In contrast, in crowded environments or when following other

pedestrians, the step length and duration of the pedestrians may vary. Thus, the randomness of the step duration of the follower is likely connected to changes in the movement of the leader. Moreover, as mentioned in Section 2.2.2, the step length of a pedestrian is influenced by that of the leader. This assumption implies that the randomness in the step duration of pedestrians is related to the variation in their step length, denoted as $\alpha_1\varepsilon_l$. Here, α_1 is a constant, and $\varepsilon_l = |l_i^{n+1} - l_i^n|/l_i^F$ measures the degree of change in the step length.

Furthermore, compared with other walking states, when $S = D$, the swing foot encounters higher resistance stepping forward, and thus, more time is required to complete this step. To account for this phenomenon, an element of randomness related to the step width is incorporated, denoted as $\alpha_2\varepsilon_w$. Here, α_2 is a constant, and $\varepsilon_w = (L_i^p - w_i^{n+1})/\left[L_i^p\left(1 - \cos\psi_p^{max}\right)\right]$ is the level of body rotation.

In general, the step duration is calculated as

$$\Delta_i^{n+1} = \max(\mathcal{T}_{low}, \mathcal{T} + \epsilon_1\alpha_1\varepsilon_l + \mathbb{I}[S^{n+1} = D]\,\epsilon_2\alpha_2\varepsilon_w) \quad (6)$$

where $\mathcal{T}(\cdot)$ is the third general function, a specific form of which is presented in Section 4.1. ϵ_1 and ϵ_2 are two independent uniform random numbers in the interval [-1, 1] and [0, 1], respectively.

It is important to note that each pedestrian in the model may have a different step duration. The methodology for determining time scales for other pedestrians follows the same approach as described for ped_i and ped_j in Fig.1. The model updates occur at regular intervals of the time step δ ($t = t + \delta$). The gait parameters, specifically the step duration, are calculated only for pedestrians whose ongoing step concludes at the current time instance. The position of other pedestrians is determined using the method outlined in Section 2.3. As the step duration, Δ, can have decimal values, the number of time steps required to complete a step is calculated by rounding the result of Δ/δ, to the nearest integer. This method ensures the consistency of the time scale by converting decimal values into integers.

For instance, let's consider two pedestrians, A and B. It is assumed that both A and B complete their steps simultaneously. Furthermore, the next step duration for A and B is 0.6 seconds and 0.75 seconds, respectively. Consequently, A's single support phase will conclude after 15 model updates, while B's single support phase will end after 18 model updates.

2.3. Single support phase

This section introduces the rules for variations in the gait parameters in the single support phase and describes a collision avoidance mechanism. During the single support phase ($t \in \left(T_i^n, T_i^{n+1}\right]$), the position of the swing foot at the end of the nth step, $P_i^{11}(T_i^n)$, becomes the position of the support foot in the $n+1$th step. Thus, all the joint positions, $P_i(t)$, are determined by both $P_i^{11}(T_i^n)$ and the gait parameter at time t, $X_i(t)$. Specifically, $P_i(t)$ is the gait resulting by the shift (represented by $\oplus$) of $\mathcal{B}\left(X_i(t)\right)$ to a position in which the support foot is at position $P_i^{11}(T_i^n)$:

$$P_i(t) = \mathcal{B}\left(X_i(t)\right) \oplus P_i^{11}(T_i^n), t \in \left(T_i^n, T_i^{n+1}\right] \tag{7}$$

2.3.1. Variation rules for gait parameters

The movement of the swing foot in the single support phase is modeled in Eq. (8). The movement along the longitudinal axis of the swing foot (i.e., the change in step length) is modeled as an acceleration process followed by deceleration (Chung et al., 2012; Huang et al., 2018), as indicated in Eq. (8d). Notably, a swing foot moves from behind a support foot to in front of it. Thus, the first term of Q is set as -1, indicating that a swing foot moves a total distance of $l^{n+1} + l^n$ during this phase. The lateral movement of the swing foot (i.e., the change in step width) and rotation of the shoulders (i.e., the change in projected shoulder width) are assumed to change uniformly. Furthermore, the orientation is assumed to change instantaneously (the fourth term of Q is set as $1 + \Delta\gamma/\gamma_i^n$), and the sway angle is

assumed to remain unchanged.

$$X_i(t) = X_i(\tau + T_i^n) = Q\, X_i(T_i^n) + \int_0^{\tau} A\,(t)\, dt \tag{8a}$$

$$Q = diag\left\{-1,1,1,1 + \frac{\Delta\gamma}{\gamma_i^n}, 1\right\} \tag{8b}$$

$$A(t) = \left[A_l(t), \frac{w_i^{n+1} - w_i^n}{\Delta_i^{n+1}}, \frac{s_i^{n+1} - s_i^n}{\Delta_i^{n+1}}, 0,0\right]^T \tag{8c}$$

$$A_l(t) = \begin{cases} \dfrac{l_i^{n+1} + l_i^n}{\left(\frac{1}{2}\Delta_i^{n+1}\right)^2}\, t & , t \in \left(0, \dfrac{1}{2}\Delta_i^{n+1}\right] \\ \dfrac{l_i^{n+1} + l_i^n}{\left(\frac{1}{2}\Delta_i^{n+1}\right)^2}\left(\Delta_i^{n+1} - t\right), t \in \left(\dfrac{1}{2}\Delta_i^{n+1}, \Delta_i^{n+1}\right] \end{cases} \tag{8d}$$

2.3.2. Collision avoidance

As discussed in Section 2.2.2, step-synchronization increases the step length of the follower. However, if the leader does not maintain the consistent walking speed anticipated by the follower, the two pedestrians may collide. Therefore, precautions must be taken to avoid such collisions.

During the single support phase of the follower, if the distance between the swing foot of the follower and center of mass of the leader is less than the sum of the shoulder projection lengths of these two pedestrians in the velocity direction of the follower, the follower is at risk of colliding with the leader, as shown in Fig. 7. In Figure 7, R is defined as $R = \max\left(b, \frac{1}{2}\sqrt{2b\sin\psi_s}\right)$, where ψ_s is the shoulder rotation angle and b is half of the body depth, set to 0.15 m (Song et al., 2019). R_i represents the value of R for ped_i. To prevent a collision, the follower prematurely ends the current step (the $n+1$th step), that is, let $l_i^{n+1} = l_i(t);\ \ w_i^{n+1} = w_i(t);\ \ s_i^{n+1} = s_i(t)$.

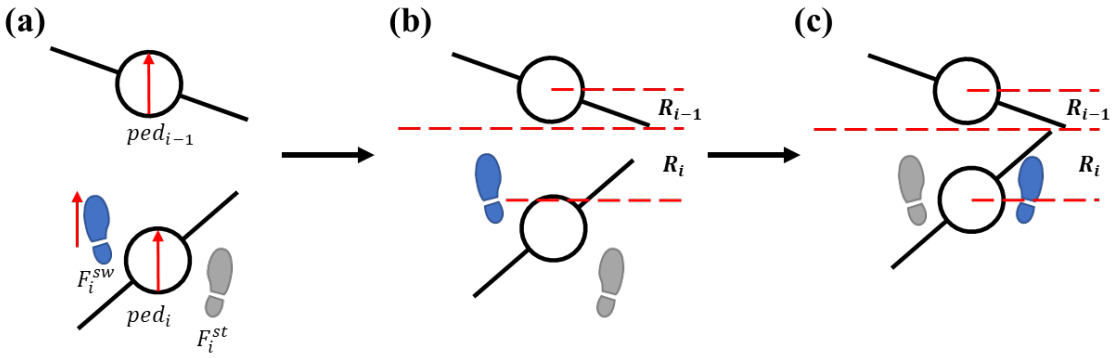

Fig. 7. Collision avoidance. The gray and blue feet represent the swing foot and support foot of ped_i, respectively. In (a), F_i^{sw} is moving forward and touches the ground as soon as it reaches the position shown in (b). Thereafter, F_i^{st} and F_i^{sw} are switched, and the gait of the next step is planned. If ped_{i-1} is not moving during this process,ped_i has a standing gait, as shown in (c). In this scenario, ped_i successfully avoids a collision with ped_{i-1}. The upper dashed line represents the arc direction location of the center of ped_{i-1} (denoted as $\mathcal{L}_1$), the middle dashed line signifies the arc direction location of $\mathcal{L}_1 + \mathrm{R_{i-1}}$, and the bottom dashed line indicates the arc direction location of $\mathcal{L}_1 + \mathrm{R_{i-1}} + \mathrm{R_i}$. The bottom dashed line marks the location where ped_i does not collide with ped_{i-1}.

3. Data collection

3.1. Experimental setup

For model calibration, two types of experiments were conducted on May 30, 2021, at Beijing Jiaotong University in China. The experiments were performed on a public square at the university, where two circular tracks with different radii were set up for single-file and narrow-corridor experiments. The single-file experiments were conducted on a track with an inner radius of 3.0 m and an outer radius of 3.7 m. The narrow-corridor experiments were conducted on a track with an inner radius of 3.1 m and an outer radius of 3.6 m. The circular track is widely used to study vehicle, bicycle, and pedestrian flow (Moussaïd et al., 2012; Guo et al., 2016). A key advantage of this track is its periodic boundary, which maintains the system density and thereby prevents the generation of disturbances, which occur in tracks with entries and exits. Two video cameras were placed on a high-rise building next to the public square to obtain an approximately top-down view, and thus each could record one of the two types of experiment. Video recordings were taken at 25 frames per second at a resolution of

1920 × 1080 pixels. Figure 8 gives snapshots of these two types of experiments.

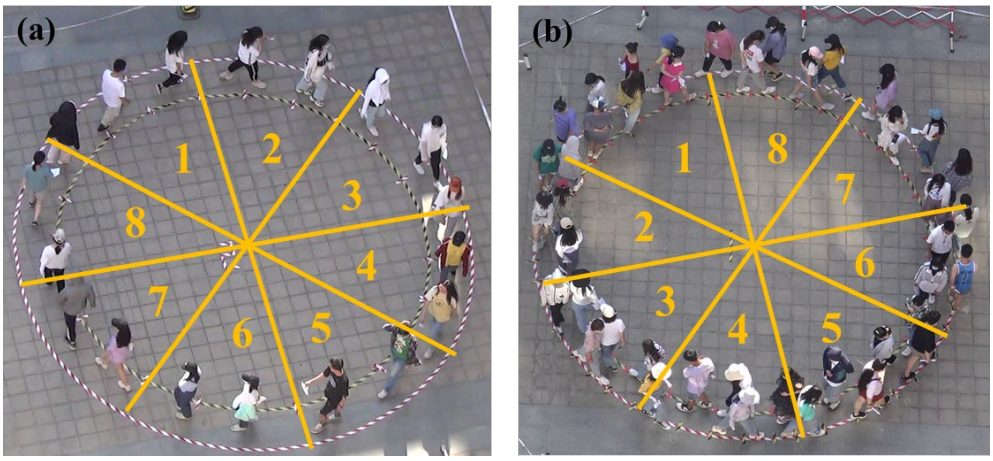

Fig. 8. Snapshots of the two types of experiment. (a) The single-file experiment of run 3-2. (b)The narrow-corridor experiment of run 7-2.

The study involved 60 participants from the university who were aged 18–26. The experiments were conducted in single-file (unidirectional) and narrow-corridor conditions (bi-directional) at nine and 10 different global densities, respectively ($N = 6, 12, \ldots, 54$ and $N = 6, 12, \ldots, 60$). Each set of experiments was conducted twice and lasted approximately 5 min. The experimental arrangement is summarized in Appendix C.

During each run, the participants were positioned uniformly in the corridor at the start and instructed to walk naturally on the circular track. Collisions and overtaking others were not allowed. Half of the participants (N/2) in the narrow-corridor experiments were instructed to walk clockwise on the inner track, while the others were instructed to walk counterclockwise on the outer track. In addition, for safety purposes, no physical boundaries were set, but the participants were instructed to carefully walk within the boundary line and rotate their bodies to avoid collisions with those walking in the opposite direction.

3.2. Measurement method

Local density and its corresponding flow rate are used to study the fundamental diagram. In Zhang

et al. (2011), local density in an area is defined as follows:

$$\rho_l = \frac{1}{\Delta t}\int_t^{t+\Delta t} \frac{N_l(t)}{s} dt \tag{9}$$

where $N_l(t)$ is the number of pedestrians in an area of size s at time t. The circular corridor is divided into eight equal subareas (see Fig. 8). Δt was set to 15 s in this experiment, and s is 1/8 of the corridor length, which was approximately 2.63 m for the single-file experiments (the middle line) and 2.43 m and 2.83 m for the inner and outer tracks, respectively, in the narrow-corridor experiments.

The corresponding local flow rate is defined as the number of pedestrians (q) crossing the subarea per unit of time (Δt), that is $f_l = q/\Delta t$. In each experiment, the first 1–2 min was a warm-up period, the data of which are excluded from the analysis.

3.3. Fundamental diagram

The relationship between flow and density is first investigated[4]. Figure 9(a) displays the scatterplot of flow-density data obtained from the single-file experiment, whereas Fig. 9(b) and (c) display the scatterplots of flow-density data obtained from the narrow-corridor experiment. A binning method (Jelić et al., 2012a; Ma et al., 2021) with a density interval of 0.2 ped/m is used to average the scatters.

Figure 9(a) illustrates the fundamental diagram of the single-file experiment. The flow initially increased with the density in the free-walking state and then decreased with a further increase in density. The maximum flow rate reached 0.96 ped/s at a critical density of approximately 0.85 ped/m.

Figure 9(b) plots the local densities and their corresponding flow rates in both the inner (orange dots) and outer (blue triangles) tracks. Despite the high variability observed in both sets of data, they exhibited similarities with the data for the single-file experiment, in which the flow rates increased and then decreased with increasing density. The statistical results from the binning method also reveal

[4] For diagram of flow rate versus pedestrian number, please refer to Appendix D

differences between the narrow-corridor experiment and the single-file experiment, see Fig. 9(c).

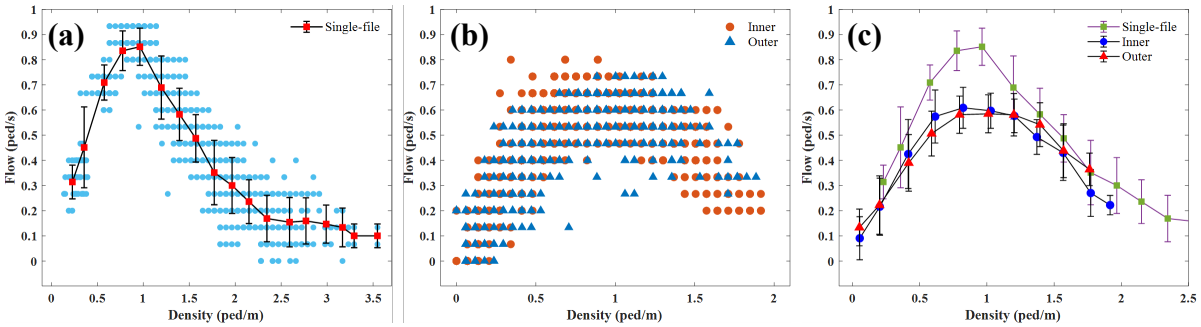

Fig. 9. Fundamental diagrams of flow rate and density obtained from (a) single-file experiments and (b) narrow-corridor experiments. (c) Average results from the single-file experiments (green squares) and those from the inner (blue dots) and outer (red triangles) tracks of the narrow-corridor experiments. The error bars represent the standard deviations of the flow rate in each density interval.

In the narrow-corridor scenario, the flow rate in the two tracks approximately consisted of three evolution stages, rather than two stages, as was observed in the single-file experiment. Initially, the outer (inner) track flow increased with density. Once the density reached approximately 0.8 ped/m (0.6 ped/m), the flow rate became relatively stable. The maximum average flow rates in the two tracks were quite similar, with that of the outer track reaching 0.58 ped/s and that of the inner track reaching 0.61 ped/s. Finally, the flow decreased with density when the density was larger than 1.2 ped/m in both tracks.

Compared with the flow rates in the single-file experiment, those in the narrow-corridor experiment remained consistently lower, in a density range from 0.22 ped/m (the minimum local density in the single-file experiment) to 1.91 ped/m (the maximum local density in the narrow-corridor experiment). Body rotation is one contributing factor to the reduction in the walking speed of the pedestrians, consequently affecting the overall flow rate.

3.4. Spatiotemporal evolution

The spatiotemporal evolution and the occurrence of stop-and-go waves are investigated by plotting the evolution of the number of pedestrians passing through eight subareas (which equals the local flow rate) and the density evolution over time for single-file experiments with 30 (run 5-2) and 54 (run 9-2)

pedestrians, and for narrow-corridor experiments with 30 pedestrians on both the inner and outer tracks (run 10-2). The data collection had at least a 1-min warm-up and obtained 3 min of data, with a time interval of 5 s.

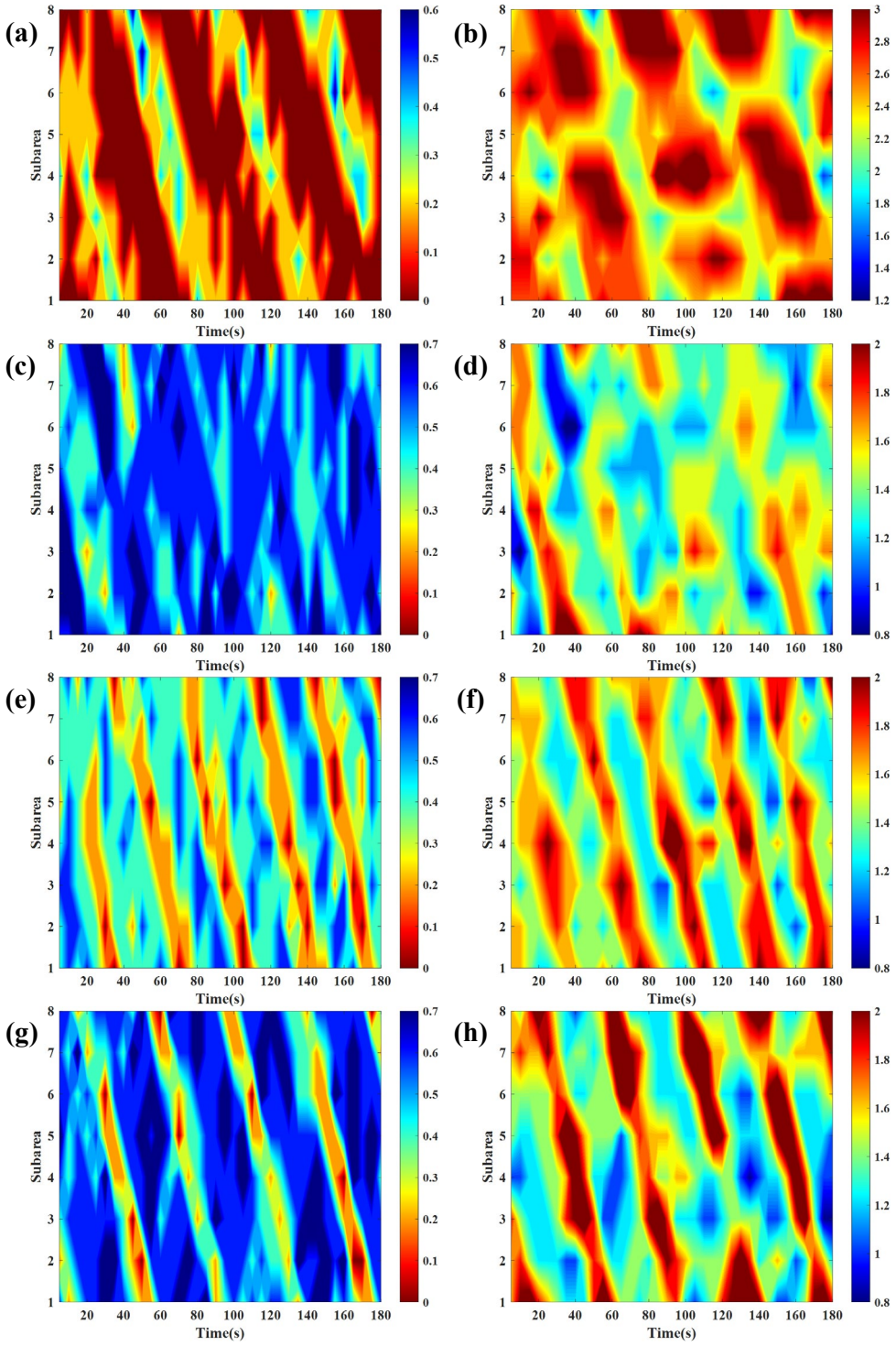

Fig. 10. Evolution of local flow rate and local density in eight subareas over time. Local flow rate and local density: (a), (b) for the single-file experiment of run 9-2; (c), (d) for the single-file experiment of run 5-2; (e), (f) for the

inner track of the narrow-corridor experiment of run 10-2; and (g), (h) for the outer track of the narrow-corridor experiment of run 10-2.

The resulting flow-rate evolution diagrams in Fig. 10(a), (e), and (g) show the occurrence of stop-and-go waves, indicating that the pedestrian flow in these experiments was not stable or uniform. Additionally, the density evolution diagrams in Fig. 10(b), (f), and (h) show the occurrence of local congestion. A comparison of the corresponding flow-rate evolution diagrams reveals that the strip representing walking corresponds to the strip representing low density, suggesting that pedestrians required more space to move forward and could tolerate closer distances to pedestrians in front when they stopped.

Furthermore, by comparing Fig. 10(c), (e), and (g), which represent the experiments with 30 pedestrians on a track (where the difference in track length can be ignored), the different natures of the two types of experiments are revealed. Although there were fluctuations in local flow rate (Fig. 10(c)) and local density (Fig. 10(d)) in the single-file experiment, there was no obvious congestion or stop-and-go wave. However, although the lengths of the inner and outer tracks were different in the narrow-corridor experiment, there was a clear stop-and-go wave on both tracks. This indicates that compared with the single-file experiment, pedestrians were more resistant to moving forward in the narrow-corridor experiment, and therefore needed to make more of an effort to take a step forward. As a result, compared with pedestrians in the single-file experiment, those in the narrow-corridor experiment tended to wait for a larger gap in front to take a longer or faster step rather than a small step. This led to the formation of a stop-and-go wave.

4. Model Specification and calibration

4.1. Specification of the general functions

Simulations are conducted considering circular tracks centered at $O \in \mathbb{R}^{3\times1}$. First, the dynamic motion of a 3D point, $p \in \mathbb{R}^{3\times1}$, is treated as the projection onto the *x*-*y* plane, denoted as $\hat{p} = [p_x, p_y, 0]^T$. A

function is defined to measure the radius of a circle with the center of p_2 and p_1 located on its edge:

$$G(p_1, p_2) = \|p_1 - p_2\| \tag{10a}$$

$$G_i = G\left(\hat{C}_i(T_i^n), \hat{O}\right), G_j = G\left(\hat{C}_j(T_i^n), \hat{O}\right), G_j^m = G\left(\hat{P}_j^m(T_i^n), \hat{O}\right), G_i^m = G\left(\hat{P}_i^m(T_i^n), \hat{O}\right) \tag{10b}$$

The following form of $\mathcal{D}(\cdot)$ is defined (Fig. 11(a)):

$$\mathcal{D}\left(C_i(T_i^n), \vec{f}_i, \gamma_i^n, P_j^7(T_i^n), P_j^9(T_i^n), O\right) = \min_{m\in\{13,15\}} \left\{ \frac{G_j - G_i}{|G_j - G_i|} \left(G_j^m - G_i\right) \right\} - dy_i^{psy} \tag{11}$$

where P^7 and P^9 are shoulder positions, as shown in Fig. 3(c). $(G_j - G_i)/|G_j - G_i|$ is an indicator that equals 1 when ped_i and ped_j are on the inner and outer tracks, respectively, and -1 when the situation is reversed. dy_i^{psy} is an indicator of the psychological tendency of ped_i to avoid physical contact.

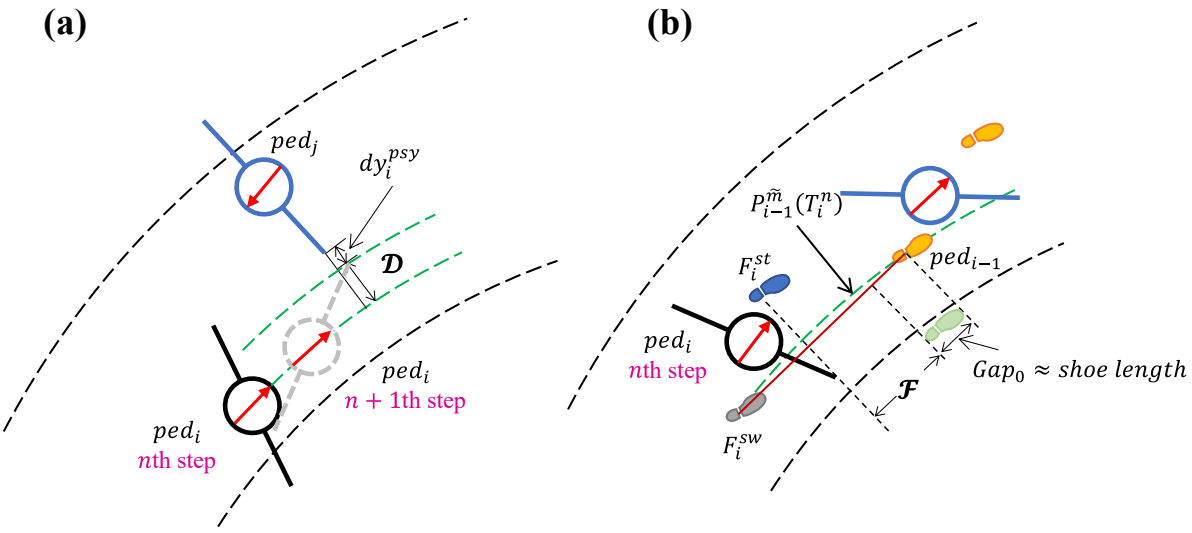

Fig. 11. Schematic for the calculation of (a) $\mathcal{D}$ and (b) $\mathcal{F}$. (a) The black and gray circles represent the position and rotated shoulders of ped_i at the end moment of the nth and $n+1$th step, respectively. The blue circle is a pedestrian walking in the opposite direction at time T_i^n. (b) The blue pedestrian is the leader of ped_i, with feet highlighted in yellow. In both subfigures, the black dashed curves denote the boundaries of the circular tracks. The green dashed curves denote concentric arcs.

The following form of $\mathcal{F}(\cdot)$is specified (Fig. 11(b)):

$$\tilde{m} = \underset{m\in\{0,11\}}{\operatorname{argmin}} \left|G_{i-1}^m - G_i^5\right| \tag{12a}$$

$$\mathcal{F}\left(P_i^5(T_i^n), \vec{f}_i, \gamma_i^n, P_{i-1}^0(T_i^n), P_{i-1}^5(T_i^n), O\right) = \max\left(0, \left\|P_{i-1}^{\tilde{m}}(T_i^n) - P_i^0(T_i^n)\right\| - Gap_0\right) \tag{12b}$$

where $\tilde{m}$ denotes the foot of ped_{i-1} at time T_i^n that is radially closer to the swing foot of ped_i; and P^0 and P^5 are the support and swing foot positions, respectively. Gap_0 is the minimum safety distance.

As mentioned in the conclusion of Section 3.4, pedestrians in the narrow-corridor experiment were seen to wait for a larger gap in front in order to take a longer or faster step, instead of taking a minimal step. This behavior is represented by the term l^{min} in Eq. (5b), where a larger body rotation angle corresponds to a larger l^{min}. To incorporate this behavior, the minimum step length for ped_i, l_i^{min}, can be expressed as:

$$l_i^{min} = l_0^{min} + \lambda \frac{\left(L_i^p - w_i^{n+1}\right)}{\left[L_i^p \left(1 - \cos \psi_p^{max}\right)\right]} \tag{13}$$

where, l_0^{min} and λ are constants. The second component of Eq.(13) is an indicator of the body rotation level and is equivalent to ε_w in Eq. (6).

In the simulation, $\mathcal{T}(\cdot)$ is assumed to be an inverse proportional function, with the argument of the step length, an upper bound of $\mathcal{T}_{upp}$, a lower bound of $\mathcal{T}_{low}$, and a constant of proportionality of α_3:

$$\mathcal{T}(l_i^{n+1}) = \min\left(\mathcal{T}_{upp}, \max\left(\mathcal{T}_{low}, \frac{\alpha_3}{l_i^{n+1}}\right)\right) \tag{14}$$

In this setting, a comparable relationship between the step frequency and headway can be reproduced, as indicated by the experimental results presented in Appendix B.

4.2. Model calibration

The height of a pedestrian, H, is a random number within the interval [1.6, 1.8] (m). The maximum stepping angle, θ_w^{max}, is also a random number within the interval [0.36, 0.4] (rad). Consequently, the maximum step length without rotation, as well as the free-walking step length, l^F, falls within the interval [0.55, 0.65] (m). With a step duration of 0.5 s, the free-walking velocity ranges between [1.2, 1.5] (m/s), which aligns with real-world observations. Gap_0 is randomly assigned a value within a range of [0.3, 0.38] (m), slightly larger than a shoe length. $\mathcal{T}_{low}$ is obtained from Fang et al. (2012), while $\mathcal{T}_{upp}$ is estimated from Huang et al. (2018).

Other parameters are calibrated using the genetic algorithm to minimize the mean squared error (defined in Appendix E) of the local flow rate between experiments and simulations. A summary of all calibrated parameters in HPM is provided in Table 6.

Table 6 Parameter values used in the simulations.

Parameter	Definition	Value	Unit
H	Pedestrian height	$[1.6, 1.8]$	m
θ_w^{max}	Maximum stepping angle	$[0.36, 0.4]$	rad
ψ_p^{max}	Maximum pelvis rotation angle	$\pi/4$	rad
ω	Sway angle	$\pi/90$	rad
D_v	Vision limitation	5.5	m
l_0^{min}	Minimum step length	0.1	m
λ	Parameter of step length	0.15	m
Gap_0	Parameter of step length	$[0.3, 0.38]$	m
d_{safe}	Parameter of synchronization	0.65	m
d_{th}	Parameter of body rotation	1.2	m
k	Parameter of body rotation	3	–
dy^{psy}	Parameter of body rotation	0.05	m
α_1	Parameter of step duration	0.15	–
α_2	Parameter of step duration	0.5	–
α_3	Parameter of step duration	0.25	–
$\mathcal{T}_{low}$	Parameter of step duration	0.5	s
$\mathcal{T}_{upp}$	Parameter of step duration	0.8	s
δ	Time step	0.04	s

5. Simulation results

5.1. Simulation of the single-file experiment

As in the single-file experiment, the number of pedestrians in the simulation ranges from N = 6 to N = 54, with an interval of 6. At the start of each run, all of the pedestrians are positioned approximately uniformly on a circular track with a radius of 3.35 m, take the first step with an arbitrary foot, and then walk in a clockwise direction. Fig. 12(a) and (b) is a snapshot of the simulation with 18 pedestrians.

Figure 12(c) shows the fundamental diagram of the simulation. As shown in Table 7, the error terms (their definitions are given in Appendix E), i.e., MSE, the root-mean-square error, the relative root-mean-square error, and the mean absolute percentage error show the goodness-of-fit. Figure 13(d)

and (e) present the evolution of local flow rate and density in eight subareas over time in the simulation with 54 pedestrians, demonstrating that the HPM can reproduce the stop-and-go wave observed in the experiment. In addition, the standard deviation of the local flow rate is evaluated in each time interval, and plot their evolution for comparison with the experimental results in Fig. 13(f). The result indicates there is good agreement between the simulation and the experiment.

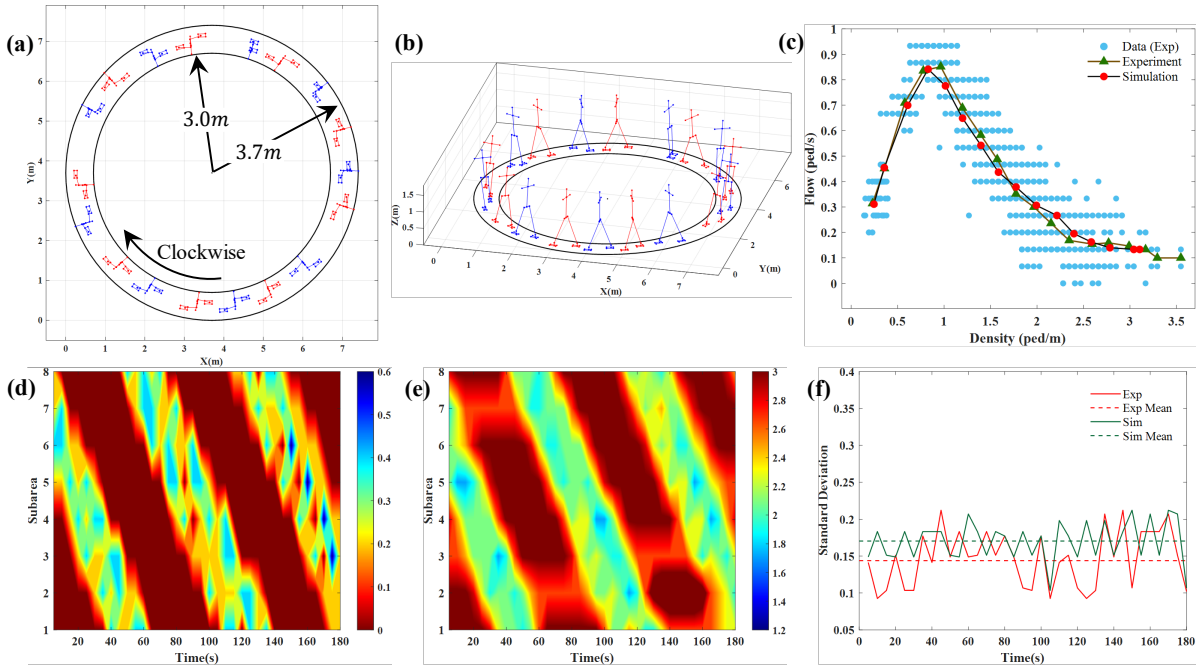

Fig. 12. Snapshots of the single-file simulation with 18 pedestrians. (a) From a superior view. (b) From an anterior view. Simulation results of the single-file scenario. (c) Fundamental diagram of the flow–density relationship. Solid lines are the experimental (green triangle) and simulation (red dot) results after the binning process, and scatter points are the experimental data. (d) The evolution of local flow rate and (e) the evolution of local density in eight subareas over time in the simulation with 54 pedestrians. (f) The evolution of the mean value and standard deviation of local flow rate with 54 pedestrians in the experiment (red line) and the simulation (green line). Dashed lines are the averaged results.

Table 7 Some errors for the experimental and simulated flow rate.

	Single-file scenario	Narrow-corridor scenario	
		Inner	Outer
MSE	0.0009	0.0013	0.0015
RMSE	0.0304	0.0359	0.0382
RRMSE	13.25%	16.87%	18.08%
MAPE	6.30%	9.90%	11.52%

5.2. Simulation of the narrow-corridor experiment

In the simulated narrow-corridor experiment, two groups of equal-sized pedestrians walk in

opposite directions within a corridor. Specifically, those on the inner track walk clockwise, while those on the outer track walk counterclockwise. The simulation includes a total of 10 different densities, ranging from 6 to 60 pedestrians, with an interval of 6, which is the same range as in the experiment. One difference between the simulation and the experiment is that in the latter, the inner and the outer track radii are set to 3.05 m and 3.65 m, respectively, which are 0.05 m smaller and larger, respectively, than in the experiment. This is because, for safety reasons, the experiment did not use physical barriers to define the narrow corridor; instead, the participants were instructed to walk within the corridor as much as possible. However, this was difficult in practice, and it was observed that participants often walked outside the corridor. In contrast, the simulation forces all of the pedestrians to walk within the narrow corridor (by requiring their right foot to always stay on the track). Therefore, the sizes of the two tracks are increased in the simulation. A snapshot of this setup is shown in Fig. 13.

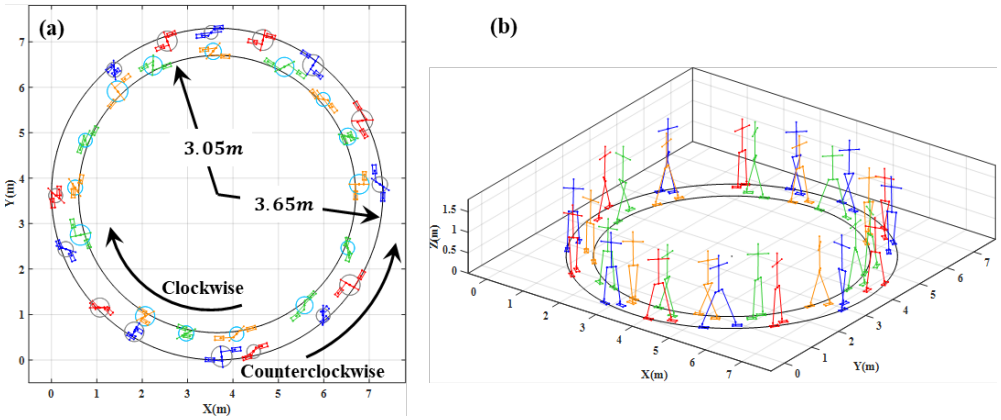

Fig. 13. Snapshots of the simulation with 30 pedestrians in the narrow corridor situation. (a) From a superior view, the radius of the circle on each pedestrian is the half of s. (b) From an anterior view.

Figure 14(a) and (b) depict the fundamental diagram of the simulation. The simulation results are consistent with the experimental results for both the inner and outer track, as evidenced by the error terms shown in Table 7. The evolution of the local flow rate in eight subareas over time in the inner and outer tracks are presented in Fig. 14(c) and (d), respectively. The corresponding evolutions of local density in the inner and outer track are depicted in Fig. 14(e) and (f), respectively.

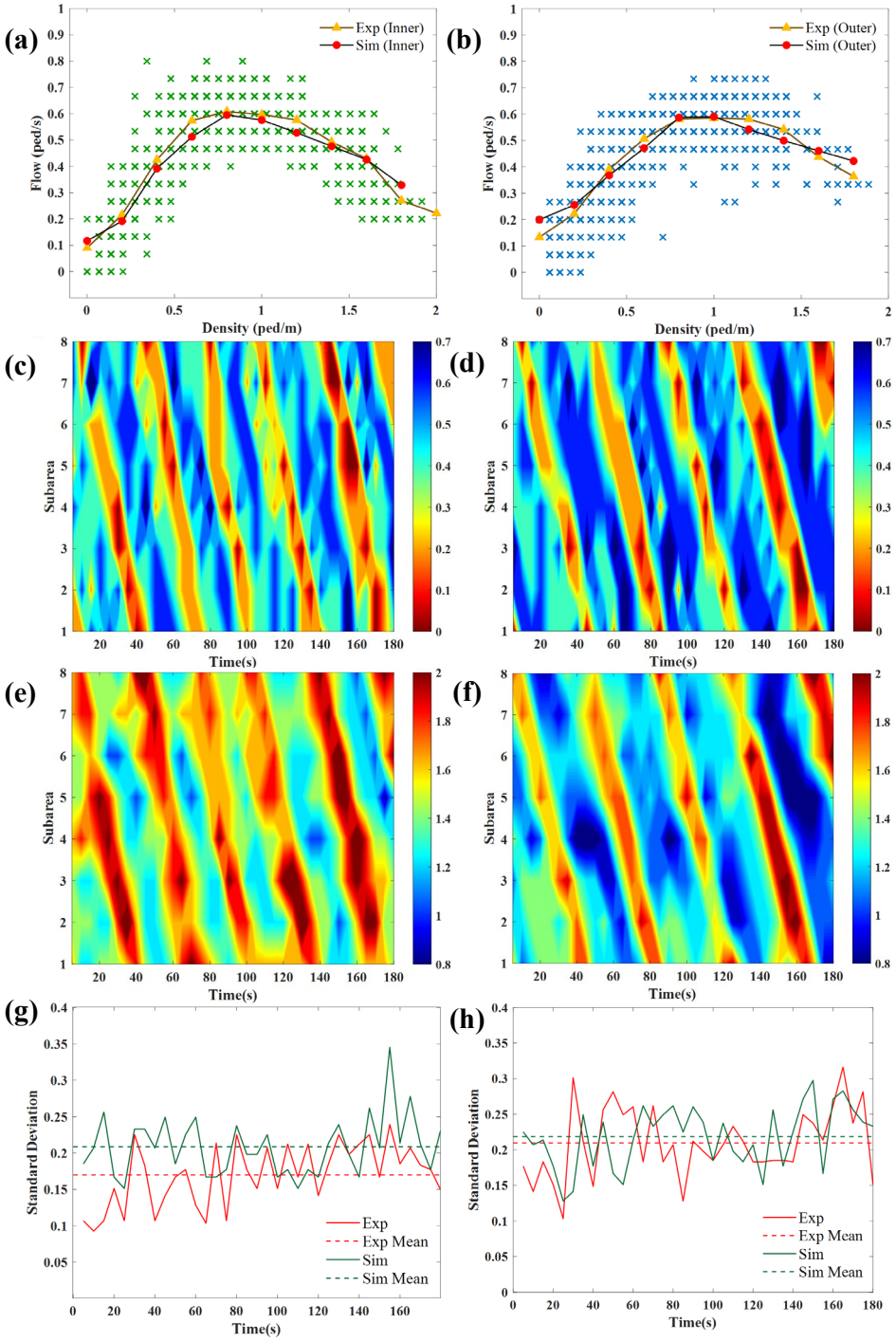

Fig. 14. Simulation results of the narrow-corridor experiment. (a), (b) Fundamental diagrams of the flow–density relationship. Solid lines are the experimental (yellow triangle) and simulation (red dot) results after the binning process, and scatter points are the experimental data. (c), (d) Evolution of local flow rate and (e), (f) evolution of local density in eight subareas over time in the simulation with 30 pedestrians. (g), (h) Evolution of the standard deviation of local flow rate with 30 pedestrians on each track. Red lines and green lines represent the experimental and simulation results, respectively. Dashed lines are the average results. The first row = inner track; the second row = outer track.

One can see that there is local congestion and a stop-and-go wave, which is similar to what occurred

in the experiment.[5] Moreover, the standard deviation of the local flow rate in each time interval is plotted and compared with the experimental results, as shown in Figure 14(g) and (h).

5.3. Step-synchronization phenomenon

This section compares the step-synchronization phenomenon in the simulation with the experimental result provided by Ma et al. (2021).

Ma et al. (2021) conducted a set of single-file experiments with seven global densities. The movements of the heads, left feet, and right feet of pedestrians were recorded using three camcorders from different viewpoints. A total of 3,439 pairs of successive pedestrians with independently complete foot cycles were detected, and 562 of these pairs were synchronized[6]. The local densities (the inverse of the headway) of the followers in these synchronized pairs were calculated and are referred to as $SynE$ in this section. $SynE$ was found to follow a log-normal distribution (see the orange line in Fig.15(a)), indicating that synchronization is most likely to be induced at a characteristic density, which was 0.87 ped/m in their experiment.

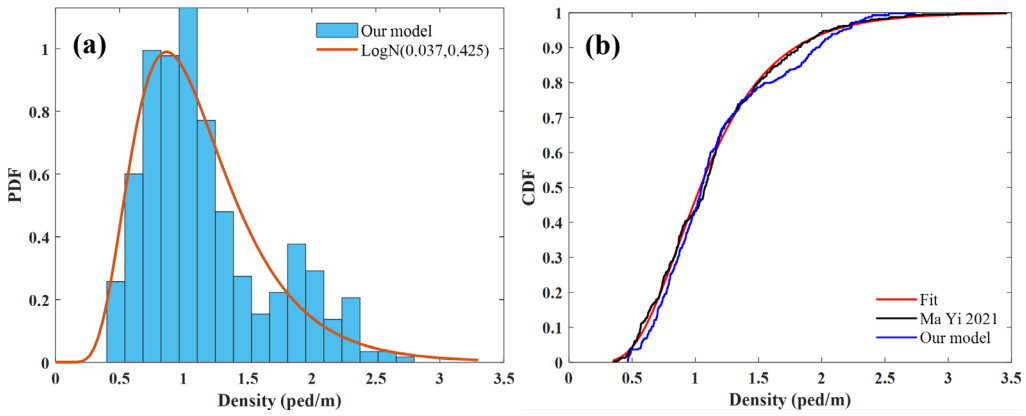

Fig. 15. Statistical results of the local densities over all 810 pairs of synchronized steps of the simulation ($SynS$). (a) Histogram plot of local densities, where the orange line is the fitted log-normal distribution of the public

[5] Appendix F displays the outcomes of not taking into account the influence of body rotation on stepping behavior. It demonstrates the significance of acknowledging this impact.

[6] In their paper, the synchronization of a single foot of two consecutive pedestrians should conform to two conditions: (1) start time conformity (i.e., $\left|t_f^s - t_p^s\right| \le K_1$); and (2) duration conformity (i.e., $\left|\Delta t_f - \Delta t_p\right| \le K_2$), where t_f^s and t_p^s (Δt_f and Δt_p) represent the start time (duration) of the step for the follower and the leader, respectively. The values of K_1 and K_2) are set to 0.1 s and $((\Delta t_f + \Delta t_p)/8$, respectively

dataset $SynE$. (b) Cumulative distribution functions (CDF) of $SynE$, $SynS$, and the fitted log-normal distribution.

The simulation of the single-file situation is analyzed using the same method as used by Ma et al. (2021). Thus, 413 pairs of steps are synchronized from runs with nine different global densities (N = 6, 12, …, 54). The dataset, consisting of the local densities of the followers of 810 pairs of synchronized steps, is referred to as $SynS$.

The statistical results of step-synchronization in the simulation are compared with those in Ma et al. (2021), as depicted in Fig. 15. The parameter μ (the mean of logarithmic values) of the log-normal distribution indicates the density that is most likely to induce step-synchronization. To focus on the difference of parameter μ, the null hypothesis is that $SynS$ and $SynE$ are from log-normal distributions with equal mean values but unknown and unequal variances. The two-sample t-test is conducted without assuming equal variances. The test result confirms that $SynS$ and $SynE$ are not significantly different (95% confidence interval, p-value $= 0.1546$).

6. Conclusion

Modeling the limb and trunk motion of pedestrians is a crucial step towards achieving a more reliable and realistic depiction of pedestrian flow compared to the current available methods. This is because the micro-characteristics at the step level, such as the periodicity of foot movement, dynamic gait adjustment, and the correlation between successive steps, have a direct impact on the macroscopic motions, such as trajectories. However, humans are complex, multi-linked machines, and walking is an intricate process that requires precise coordination of multiple body joints. Consequently, accurately and efficiently determining the positions of body joints for a large number of pedestrians poses a challenging and crucial problem.

This study introduces the Humanoid Pedestrian Model (HPM), which incorporates both stepping behavior and body rotation. To the best of the authors' knowledge, this is the first pedestrian model that

takes into account the impact of body rotation on stepping behavior. The HPM represents a pedestrian as a 3D skeleton with 11 degrees of freedom and utilizes the Denavit-Hartenberg (D-H) method to calculate the positions of body joints. These joint positions are functionally related to critical gait parameters such as step length, step width, projected shoulder width, sway angle, and orientation. In Section 2.1, the model is described as providing an elegant and universal approach to explain the mathematical correlations between joint rotation angles and walking posture. It can be applied to various walking postures. For example, walking sideways can be characterized as a posture with a step length of zero and a wider step width. Furthermore, this study introduces a pedestrian flow framework that incorporates a gait planning process. This framework includes step-synchronization behavior during the double support phase and collision avoidance during the single support phase, thereby enhancing the realism of the HPM. As an initial step, this study focuses on 1D walking behavior, specifically the behavior of pedestrians walking along a predetermined route.

Two types of experiments were conducted to verify the model. The first involved nine sets of single-file experiments and simulations under the same conditions. Comparing the fundamental diagram and the stop-and-go wave demonstrates that the simulation results are in good agreement with the experimental results. Furthermore, the local densities of two synchronized successive pedestrians are counted and compared with the public dataset. The simulation results and the dataset remain the same. The second set of experiments involved 10 narrow-corridor scenarios in which pedestrians were instructed to walk clockwise or counterclockwise in a 0.5-m-wide circular corridor and avoid collisions by rotating their bodies. The simulation results are consistent with the experimental results.

However, while the HPM performs well when considering single-file and narrow-corridor scenarios, there is still room for improvement. For example, in this study, 1D situations in which

pedestrians are in a line are considered, and their walking directions are mostly fixed. A further detailed investigation involving experiments and simulations is needed to understand stepping characteristics in higher-dimensional situations. Accordingly, in future work, the extension of the HPM to 2D scenarios will be explored.

Acknowledgments

This work was supported by grants from the National Natural Science Foundation of China (Project Nos. 72288101 and 71931002), and the Research Grants Council of the Hong Kong Special Administrative Region, China (Project No. 17201318). The third author was also supported by Francis S Y Bong Professorship in Engineering.

References

Alaska, Y. A., Aldawas, A. D., Aljerian, N. A., Memish, Z. A., Suner, S., 2017. The impact of crowd control measures on the occurrence of stampedes during Mass Gatherings: The Hajj experience. Travel Med. Infect. Dis. 15, 67–70.

Alonso-Marroquín, F., Busch, J., Chiew, C., Lozano, C., Ramírez-Gómez, Á., 2014. Simulation of counterflow pedestrian dynamics using spheropolygons. Phys. Rev. E 90 (6), 063305.

Bacik, K. A., Bacik, B. S., Rogers, T., 2023. Lane nucleation in complex active flows. Science, 379 (6635), 923–928.

Best, A., Narang, S., Manocha, D., 2016. Real-time reciprocal collision avoidance with elliptical agents. In Proc. IEEE Int. Conf. Robot. Automat. 298–305.

Blue, V. J., Adler, J. L., 2001. Cellular automata microsimulation for modeling bi-directional pedestrian walkways. Transp. Res. Part B: Methodol. 35 (3), 293–312.

Burkle, F. M., Hsu, E. B., 2011. Ram Janki Temple: understanding human stampedes. The Lancet 377

(9760), 106–107.

Chraibi, M., Seyfried, A., Schadschneider, A., 2010. Generalized centrifugal-force model for pedestrian dynamics. Phys. Rev. E 82 (4), 046111.

Chung, W., Kim, H., Yoo, Y., Moon, C.-B., Park, J., 2012. The detection and following of human legs through inductive approaches for a mobile robot with a single laser range finder. IEEE Trans. Ind. Electron. 59 (8), 3156–3166.

Denavit, J., Hartenberg, R. S., 1955. A kinematic notation for lower-pair mechanisms based on matrices. ASME. J. Appl. Mech. 22 (2), 215–221.

Dietrich, F., Köster, G., 2014. Gradient navigation model for pedestrian dynamics. Phys. Rev. E 89 (6), 1–8.

Fang, Z. M., Song, W. G., Liu, X., Lv, W., Ma, J., Xiao, X., 2012. A continuous distance model (CDM) for the single-file pedestrian movement considering step frequency and length. Physica A 391 (1–2), 307–316.

Faraji, S., Ijspeert, A. J., 2017. 3LP: A linear 3D-walking model including torso and swing dynamics. Int. J. Robotics. Res. 36 (4), 436–455.

Farina, F., Fontanelli, D., Garulli, A., Giannitrapani, A., Prattichizzo, D., 2017. Walking ahead: The headed social force model. PLOS One 12 (1), e0169734.

Guo, N., Hao, Q. Y., Jiang, R., Hu, M. Bin, Jia, B., 2016. Uni- and bi-directional pedestrian flow in the view-limited condition: Experiments and modeling. Transp. Res. Part C: Emerging Technol. 71, 63–85.

Haghani, M., Sarvi, M., 2018. Crowd behaviour and motion: Empirical methods. Transp. Res. Part B: Methodol. 107, 253–294.

Helbing, D., Buzna, L., Johansson, A., Werner, T., 2005. Self-organized pedestrian crowd dynamics: Experiments, simulations, and design solutions. Transp. Sci. 39(1), 1–24.

Helbing, D., Farkas, I., Vicsek, T., 2000. Simulating dynamical features of escape panic. Nature 407 (6803), 487–490.

Helbing, D., Johansson, A., Al-Abideen, H. Z., 2007. Dynamics of crowd disasters: An empirical study. Phys. Rev. E 75 (4), 046109.

Helbing, D., Molnár, P., 1995. Social force model for pedestrian dynamics. Phys. Rev. E 51 (5), 4282–4286.

Hidalgo, R. C., Parisi, D. R., Zuriguel, I., 2017. Simulating competitive egress of noncircular pedestrians. Phys. Rev. E 95 (4), 042319.

Hoogendoorn, S. P., Daamen, W., 2005. Pedestrian behavior at bottlenecks. Transp. Sci. 39(2), 147–159.

Huang, Z., Chraibi, M., Song, W. G., 2018. Simulation of pedestrian single-lane movement by a biped model. Phys. Rev. E 98 (4), 042309.

Jelić, A., Appert-Rolland, C., Lemercier, S., Pettré, J., 2012a. Properties of pedestrians walking in line: Fundamental diagrams. Phys. Rev. E 85 (3), 036111.

Jelić, A., Appert-Rolland, C., Lemercier, S., Pettré, J., 2012b. Properties of pedestrians walking in line. II. Stepping behavior. Phys. Rev. E 86 (4), 046111.

Jin, C. J., Jiang, R., Yin, J. L., Dong, L. Y., Li, D., 2017. Simulating bi-directional pedestrian flow in a cellular automaton model considering the body-turning behavior. Physica A 482, 666–681.

Johansson, A., Batty, M., Hayashi, K., Al Bar, O., Marcozzi, D., Memish, Z. A., 2012. Crowd and environmental management during mass gatherings. Lancet Infect. Dis. 12 (2), 150–156.

Kirchner, A., Schadschneider, A., 2002. Simulation of evacuation processes using a bionics-inspired cellular automaton model for pedestrian dynamics. Physica A 312 (1–2), 260–276.

Kuo, A. D., 1999. Stabilization of lateral motion in passive dynamic walking. Int. J. Robot. Res, 18 (9), 917–930.

Langston, P. A., Masling, R., Asmar, B. N., 2006. Crowd dynamics discrete element multi-circle model. Saf. Sci. 44 (5), 395–417.

Liang, H., Du, J., Wong, S. C., 2021. A continuum model for pedestrian flow with explicit consideration of crowd force and panic effects. Transp. Res. Part B: Methodol. 149, 100–117.

Ma, Y., Lee, E. W. M., Shi, M., Yuen, R. K. K. 2021. Spontaneous synchronization of motion in pedestrian crowds of different densities. Nat. Hum. Behav. 2021, 5 (4), 447–457.

Ma, Y., Sun, Y. Y., Lee, E. W. M., Yuen, R. K. K. 2018. Pedestrian stepping dynamics in single-file movement. Phys. Rev. E, 98 (6), 062311.

Miyagawa, D., Ichinose, G., 2020. Cellular automaton model with turning behavior in crowd evacuation. Physica A 549, 124376.

Moussaïd, M., Guillot E, G., Moreau, M., Fehrenbach, J., Chabiron, O., Lemercier, S., Pettre, J., Appert-Rolland, C., Degond, P., Theraulaz, G., 2012. Traffic instabilities in self-organized pedestrian crowds. PLOS Comput. Biol. 8 (3), e1002442.

Moussaïd, M., Helbing, D., Theraulaz, G., 2011. How simple rules determine pedestrian behavior and crowd disasters. Proc. Natl. Acad. Sci. 108 (17), 6884–6888 .

Murakami, H., Feliciani, C., Nishiyama, Y., Nishinari, K., 2021. Mutual anticipation can contribute to self-organization in human crowds. Sci. Adv. 7 (12), eabe7758.

Nakatsuka, T., Miyake, T., Kikuchi, K., Kobayashi, A., Hayashi, Y., 2019. Analyzing human avoidance

behavior in narrow passage. In Proc. IEEE Int. Conf. Syst. Man, Cybern. 3738-3743.

Narang, S., Best, A., Manocha, D., 2017. Interactive simulation of local interactions in dense crowds using elliptical agents. J. Stat. Mech: Theory Exp. 2017 (3), P033403.

Nicolas, A., Bouzat, S., Kuperman, M. N., 2017. Pedestrian flows through a narrow doorway: Effect of individual behaviours on the global flow and microscopic dynamics. Transp. Res. Part B: Methodol. 99, 30–43.

Nikolić, M., Bierlaire, M., De Lapparent, M., Scarinci, R., 2019. Multiclass speed-density relationship for pedestrian traffic. Transp. Sci. 53(3), 642–664.

Seitz, M. J., Dietrich, F., Köster, G., 2015. The effect of stepping on pedestrian trajectories. Physica A 421 (1), 594–604.

Seitz, M. J., Köster, G., 2012. Natural discretization of pedestrian movement in continuous space. Phys. Rev. E 86 (4), 046108.

Song, X., Xie, H., Sun, J., Han, D., Cui, Y., Chen, B., 2019. Simulation of pedestrian rotation dynamics near crowded exits. IEEE Trans. Intell. Transp. Syst. 20 (8), 3142–3155.

Su, B., Andelfinger, P., Eckhoff, D., Cornet, H., Marinkovic, G., Cai, W., Knoll, A., 2019. An agent-based model for evaluating the boarding and alighting efficiency of autonomous public transport vehicles. In Computational Science – ICCS 2019. 11536. DOI: 10.1007/978-3-030-22734-0_39.

von Sivers, I., Köster, G., 2015. Dynamic stride length adaptation according to utility and personal space. Transp. Res. Part B: Methodol. 74, 104–117.

Wageningen-Kessels, F., Daamen, W., Hoogendoorn, S. P., 2018. Two-dimensional approximate Godunov scheme and what it means for continuum pedestrian flow models. Transp. Sci. 52(3), 547–563.

Wang, J., Boltes, M., Seyfried, A., Zhang, J., Ziemer, V., Weng, W., 2018. Linking pedestrian flow characteristics with stepping locomotion. Physica A 500, 106–120.

Xu, Q., Chraibi, M., Tordeux, A., Zhang, J., 2019. Generalized collision-free velocity model for pedestrian dynamics. Physica A 535, 122521.

Yamamoto, H., Yanagisawa, D., Feliciani, C., Nishinari, K., 2019. Body-rotation behavior of pedestrians for collision avoidance in passing and cross flow. Transp. Res. Part B: Methodol. 122, 486–510.

Zeng, G., Cao, S., Liu, C., Song, W., 2018. Experimental and modeling study on relation of pedestrian step length and frequency under different headways. Physica A 500, 237–248.

Zhang, J., Klingsch, W., Schadschneider, A., Seyfried, A., 2011. Transitions in pedestrian fundamental diagrams of straight corridors and T-junctions. J. Stat. Mech: Theory Exp. 2011 (6), P06004.

Appendix A. Simulation without active step-synchronization

In this appendix, we will demonstrate the necessity of the step synchronization settings described in Section 2.2.2. One piece of evidence supporting this is the flow-density relationship. When all settings remain the same as in the paper, but pedestrians are not assumed to actively synchronize their steps with their leaders, the maximum flow rate decreases significantly, as illustrated in Fig. A1.

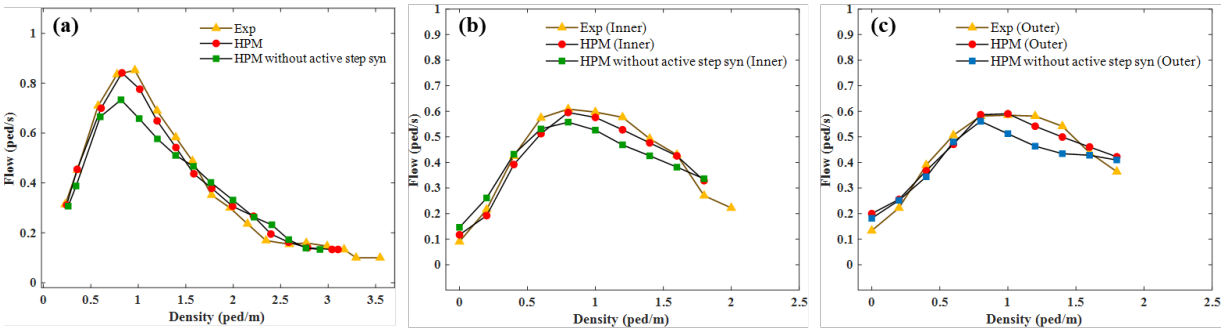

Fig. A1: The flow-density relationship without step synchronization rules is presented in (a) the single-file scenario, and (b) the inner and (c) the outer tracks of the narrow-corridor scenario. Three lines represent the experimental data (yellow triangles), simulation results of HPM (red dots), and HPM results without active step synchronization (blue squares).

Appendix B. Simulation result of the headway-step frequency relationship

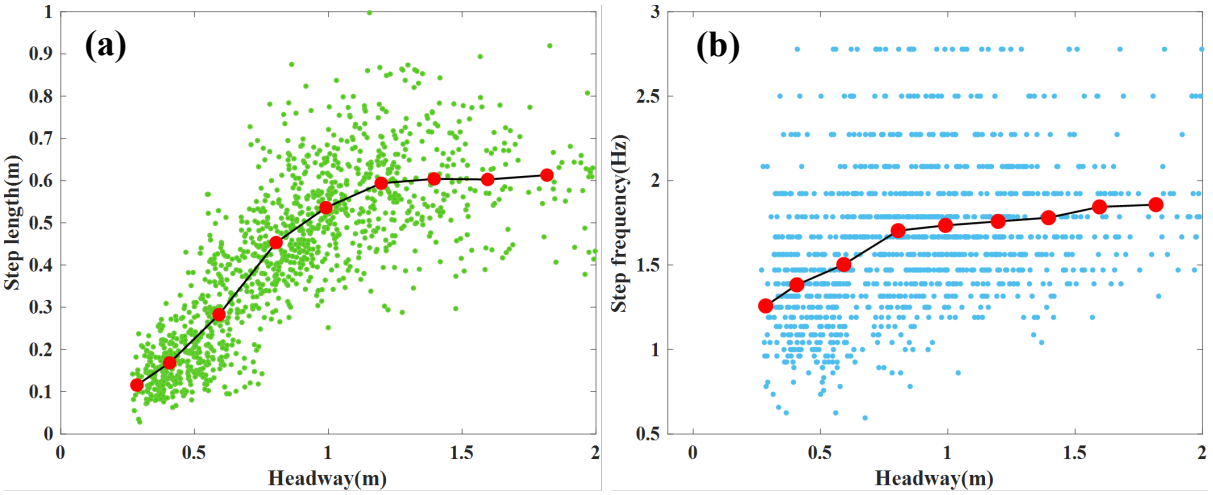

Fig. B1. Fitting result of (a) the headway–step length relationship and (b) the headway–step frequency relationship. The scatter points represent the experimental data obtained from Zeng et al. (2018). There is a greater degree of variability in step frequency (duration) compared to step length.

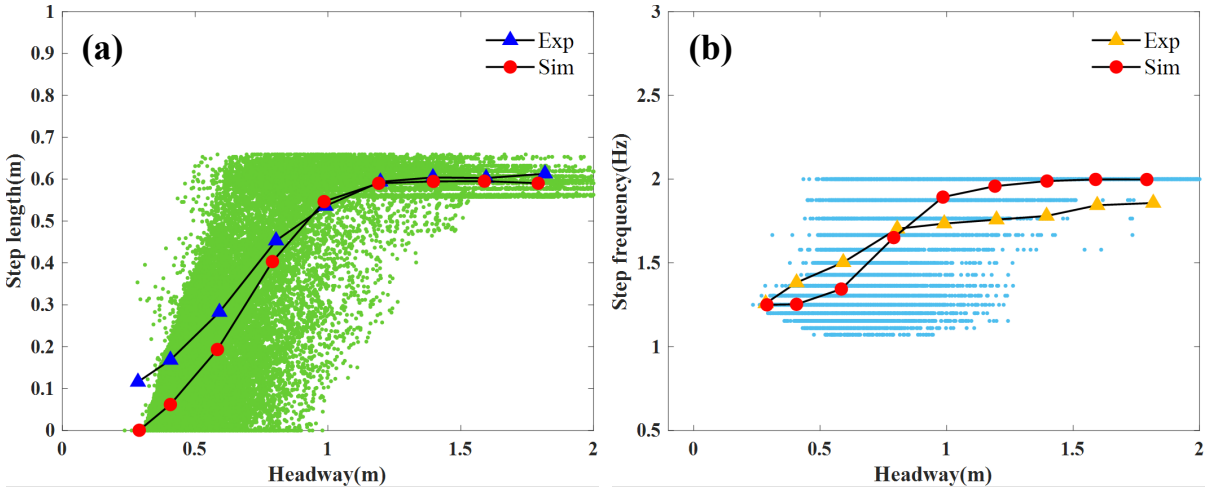

Fig. B2: Simulation results of (a) the relationship between step length and headway and (b) the relationship between step frequency and headway. Solid lines represent the experimental (triangle) and simulation (dot) results after the binning process. Scatter points correspond to the simulation data.

A simulation of the single-file situation was conducted using the same parameters provided in Table 6. The resulting relationship between step length (step frequency) and headway, depicted in Fig. B2, is qualitatively consistent with the findings from Zeng et al. (2018) in their experimental study (see Fig. B1).

Appendix C. Experimental arrangement

Table C1 summarizes the experimental arrangement. The second number of the run name indicates the run's order. For instance, "6-2" refers to the second run of the single-file experiment involving 36 participants, or the second run of the narrow-corridor experiment with 18 participants in each track.

Table C1 Experimental arrangement.

Run number	Single-file experiment		Narrow-corridor experiment		
	Number of participants	Experiment duration (min)	Number of participants in the inner track	Number of participants in the outer track	Experiment duration (min)
1-1(2)	6	5	3	3	5
2-1(2)	12	5	6	6	5
3-1(2)	18	5	9	9	5
4-1(2)	24	5	12	12	5
5-1(2)	30	5	15	15	5
6-1(2)	36	5	18	18	5

7-1(2)	42	5	21	21	5
8-1(2)	48	6	24	24	6
9-1(2)	54	6	27	27	6
10-1(2)	---	---	30	30	6

Appendix D. Results of flow rate versus pedestrian number

The diagram of flow rate versus pedestrian number is plotted in Fig. D1. One can see that the maximum flow rate is achieved when the pedestrian number is about 18 under both single file experiment and narrow corridor experiment. We plot the spatiotemporal diagram of both single file experiment and narrow corridor experiment with pedestrian number 18, see Fig. D2. One can see that the standard deviations are quite similar in both experiments, indicating that pedestrian flow patterns are consistent. Therefore, the narrower corridor does not result in higher local densities compared to the single-file configuration.

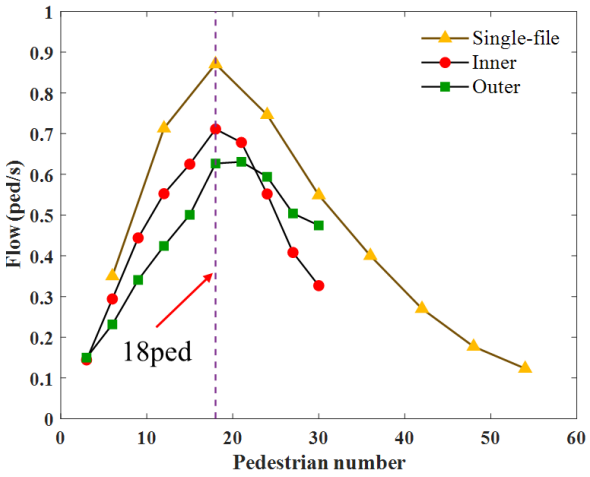

Fig.D1: Flow rate versus pedestrian number. The data points represent averages obtained from the single-file experiments (yellow triangle) and those from the inner (red dot) and outer (green square) tracks of the narrow-corridor experiments.

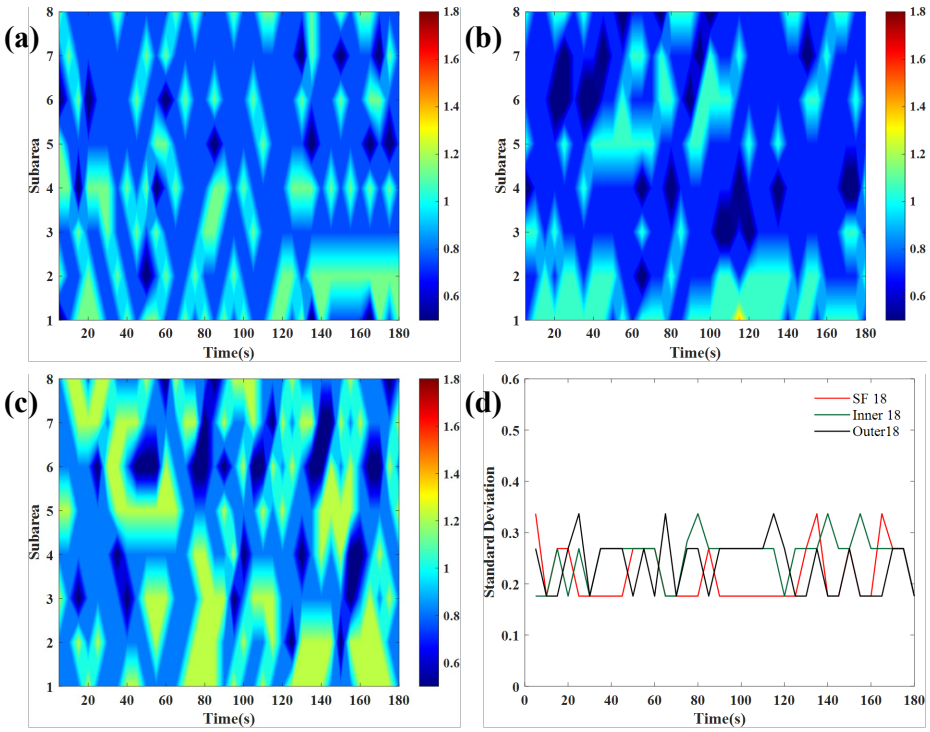

Fig. D2: The evolution of local density with 18 pedestrians in (a) the single-file experiment, (b) the outer track and (c) the inner track of the narrow-corridor experiment. (d) The evolution of standard deviations.

Appendix E. Definition of error terms

Error terms are employed to evaluate the difference between the experiment and the simulation in the fitted flow-density relationships.

Mean square error (MSE), root mean square error (RMSE), relative root mean square error (RRMSE), and mean absolute percent error (MAPE) are computed using the following formulae:

$$MSE = \frac{1}{M}\sum_{i=1}^{M}\left(y_i^{exp} - y_i^{\mathrm{sim}}\right)^2 \tag{D1}$$

$$RMSE = \sqrt{\frac{1}{M}\sum_{i=1}^{M}\left(y_i^{exp} - y_i^{\mathrm{sim}}\right)^2} \tag{D2}$$

$$RRMSE = \frac{\sqrt{\frac{1}{M}\Sigma_{i=1}^{M}\left(y_i^{exp} - y_i^{\mathrm{sim}}\right)^2}}{\sqrt{\frac{1}{M}\Sigma_{i=1}^{M}\left(y_i^{exp}\right)^2}} \tag{D3}$$

$$MAPE = \frac{1}{M}\sum_{i=1}^{M}\left|\frac{y_i^{exp} - y_i^{\mathrm{sim}}}{y_i^{exp}}\right| \tag{D4}$$

where y_i^{exp} (y_i^{sim}) is the experimental (simulation) averaged flow rate at the i-th density interval, and M is the number of density intervals.

Appendix F. Simulation disregarding the influence of body rotation on stepping behavior

In this appendix, we performed simulations neglecting the impact of body rotation on stepping behavior. The parameters were kept consistent with those outlined in the manuscript (except d_{th}, k, α_2, λ, and dy^{psy}).

Figure F1(a) and (b) shows the flow-density relationship of the narrow corridor scenario. In both Fig. F1(a) and (b), the simulation displays a higher flow rate compared to the experiment, under the same local density. Figure F1(c)-(f) displays the simulation results of flow and density evolution. It is evident from the figure that the stop-and-go wave does not occur in either the inner or outer tracks. This observation confirms the essential impact of body rotation on stepping behavior.

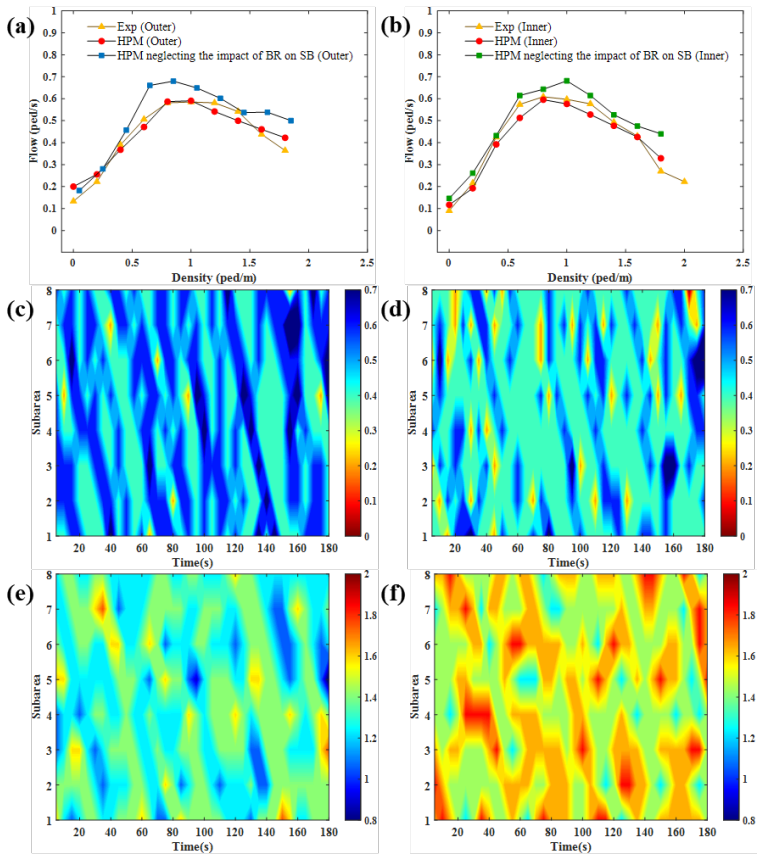

Fig. F1: Simulation results with HPM neglecting the impact of body rotation (BR) on stepping behavior (SB): (a), (b) The flow-density relationship. Three lines are the experimental results (yellow triangle), simulation results obtained using HPM (red dot), and simulations with HPM that neglects the impact of BR on SB (square). Spatiotemporal diagrams for the simulation with HPM neglecting the impact of BR on SB: (c), (d) Evolution of local flow rate and (e), (f) evolution of local density in eight subareas over time with 30 pedestrians in the track. (c),(e) outer track; (d),(f) inner track.